K. Yamazaki[1,2†], S. Aoki[1], K. Mizobata[3]

[1] Institute of Low Temperature Science, Hokkaido University, Hokkaido, Japan.

[2] Graduate School of Environmental Science, Hokkaido University, Hokkaido, Japan.

[3] Tokyo University of Marine Science and Technology, Tokyo, Japan.

Corresponding author: Kaihe Yamazaki (kaiheyamazaki@gmail.com)

† Address from 2022 Apr: National Institute of Polar Research, Tokyo, Japan.

Key Points:

- Eddy diffusivity in the Antarctic margin is 100–500 m^2 s^{-1}, likely enhanced where the recirculating gyres localize the onshore CDW flux.
- Onshore CDW flux is ~3.6 TW in the eastern Indian sector, consistent with coastal heat sinks by surface freezing and glacial melt.
- Isopycnal thickness gradient is a good predictor of mixing length and eddy diffusivity.

Abstract

Warm, salty Circumpolar Deep Water (CDW) has long been regarded as the climatological driver for Antarctica, but the mechanism of how it can reach the continental shelf remains unsettled. Motivated by the absence of observational eddy flux estimation in the Antarctic margin, we quantify isopycnal diffusivity of CDW by hydrographic records and satellite altimetry under the mixing length framework. For comparison, spiciness and thickness are used as the isopycnal tracer. Over the extent of the Antarctic Circumpolar Current (ACC), we find a general agreement with the mixing suppression theory and its exception in the lee of the topography as previously reported. In contrast, mixing length does not depend on mean flow to the pole, reflecting a stagnant flow regime in the Antarctic margin. Estimated isopycnal diffusivity ranges 100–500 m^2 s^{-1} to the south of the ACC. Eddy diffusion is likely enhanced where the CDW intrusion is localized by the recirculating gyres, primarily attributable to the small gradient of isopycnal thickness. Volume transport is then estimated by the layer thickness gradient. Associated onshore heat flux across the continental slope by CDW is calculated as ~3.6 TW and ~1.2 TW in the eastern and western Indian sectors, respectively. The estimates are quantitatively consistent with cryospheric heat sinks by sea ice formation and ice shelf basal melt, suggesting that the isopycnal eddy diffusion is the leading cause of the onshore CDW intrusion. We emphasize that the thickness field is essential for determining the eddy fluxes in the Antarctic margin.

Plain Language Summary

CDW is a significant source of heat and salt for the Antarctic coasts, so its behavior is topical for a wide range of climate sciences: especially in the contexts

of Antarctic glacial melting, sea ice variability, and global ocean overturning. Numerical simulations have previously suggested that CDW is transported onshore by advection of ocean eddies, but there has been no observational basis. Synthesizing in-situ pressure/temperature/salinity measurements and satellite altimetry, we provide a rigorous estimate of the onshore CDW transport. Shoreward heat flux by CDW eddies is generally balanced with heat loss expected by surface freezing and glacial melt, indicating that the eddy transport plays a fundamental role in the coastal heat supply. The gradient of CDW thickness primarily controls the ability to mix, i.e., spatially homogeneous thickness allows for ease of mixing. Our results facilitate a possibility to predict the eddy diffusivity solely from the layer thickness. This idea is valuable for simulating CDW transport in global climate models, where subgrid, unresolved effects of eddies need to be parameterized.

1 Introduction

Over the extent of the Antarctic Circumpolar Current (ACC), mesoscale eddies transport water masses across the streamlines, building up the adiabatic pathway of the global meridional overturning circulation (Marshall and Radko, 2003; Cessi, 2019). Isopycnal eddy diffusion is fundamental for the poleward heat flux in the Southern Ocean because the bottom enhanced diapycnal mixing (Kunze et al., 2006) and the surface water transformation (Abernathey et al., 2016) unlikely penetrates the intermediate and deep layers in the interior. Recent observations have indicated that mesoscale eddy plays a key role in bridging the Antarctic meridional overturning from deep ocean basins to the continental shelves (Thompson et al., 2014; Mckee et al., 2019), while the eddy condition from the ACC to the shoreward Antarctic Slope Current (ASC; Thompson et al., 2018) remains unconstrained.

Circumpolar Deep Water (CDW), the primary source of heat and salt for the Antarctic coasts, is transported across the ASC predominantly by mesoscale eddies in the absence of large-scale zonal pressure gradient (Stewart and Thompson, 2013). In reality, pressure gradient associated with topographic features generates standing eddies and meanders, facilitating the meridional water exchange (e.g., Hogg and Blundell, 2006). Topography-controlled geostrophic flows can transport CDW poleward in the continental margin (Morrison et al., 2020; Hirano et al., 2021). Meanwhile, the steep barotropic potential vorticity (PV) gradient on the upper continental slope (inshore of ~3,000 m isobaths) unlikely allows for the presence of the cross-slope mean flow, and hence eddy diffusion and/or tidal mixing might be essential for the onshore CDW flux near the shelf break (Stewart et al., 2018; Yamazaki et al., 2020). To the south of the ACC, the spatial distribution of eddy diffusion is yet to be described except few analyses (Foppert et al., 2019; FRE19 henceforth). From an observational standpoint, this study quests (1) to delineate the controlling factor of eddy diffusion in the Antarctic margin (portrayed as a poleward extension of Naveira Garabato et al., 2011; GFP11 henceforth) and (2) to quantify the isopycnal CDW flux by eddy diffusion towards the continental shelves.

The horizontal circulation in the Antarctic margin is shaped by the eastward ACC and the westward ASC, and in the transition zone between them exist clockwise subpolar gyres (e.g., Park and Gamberoni, 1995). The Weddell and Ross gyres are wide enough to isolate cold shelves from warm CDW, whereas ACC's proximity to the continent creates the eastward slope current in the eastern Pacific sector (Spence et al., 2017; Thompson et al., 2020) and standing eddies in the Indian sector (Mizobata et al., 2020; Yamazaki et al., 2020), resulting in the relatively warmer coastal conditions than the other sectors (Jenkins et al., 2016; Silvano et al., 2016). A lack of knowledge on the subpolar ocean circulation motivates further reanalysis of in-situ observations. Although FRE19 inferred the along-slope variability of eddy transport over the continental slope using seal-mounted conductivity-temperature-depth (CTD) data, the correspondence between the flow regime and eddy diffusion remains unclear. The present study approaches this question regarding the importance of eddy flux for the multidecadal change in the Antarctic thermal conditioning (Yamazaki et al., 2021). The East Antarctic margin (30–160°E; Fig. 1) is mainly targeted, where a sufficient amount of in-situ data exists thanks to ceaseless efforts of deploying profiling float and biologging. In this region, the eddy condition has recently been explored (FRE19; Stewart et al., 2018, 2019), lateral tidal mixing is weaker than the rest of the Antarctic margin (Beckman and Pereira, 2003), the frontal structure of ASC is relatively prominent (Pauthenet et al., 2021), and the onshore CDW flux collects attention for the future climate projection (Yamazaki et al., 2021; Hirano et al., 2021).

This paper is set out as follows. In Section 2, we review the theoretical background for observation-based eddy diffusivity calculation and introduce the concept of mixing length framework. In Section 3, we describe data and methods used for diffusivity calculation. In Section 4, mixing length, eddy diffusivity, and eddy fluxes are quantified, and their spatial variations are delineated with respect to the topographic structure in the continental margin. In Section 5, validity of presented results is assessed, and controlling factors of eddy diffusion are discussed. We conclude in Section 6.

2 Theoretical background

This section briefly reviews arguments of the mixing length framework, which provides the basis for our analysis. The observational estimates of oceanic eddy diffusion may branch in four ways: hydrographic variability (Armi and Stommel, 1983; GFP11), altimetric eddy scaling (Klocker and Abernathey, 2014; Bates et al., 2014), tracer patch deformation (Marshall et al., 2006), and dispersion time scale (LaCasce and Bower, 2000; Sallée et al., 2011). For the first two methods, the diffusivity k is derived via the mixing length formulation (Taylor, 1921):

$$k \;=\; \Gamma U_{\mathrm{eddy}} L_{\mathrm{mix}} \qquad (1),$$

where Γ is mixing efficiency (sometimes referred to as eddy transfer coefficient), U_{eddy} is characteristic eddy velocity measured by the standard deviation of

downgradient velocity $\sigma(v)$, and L_{mix} is mixing length scale. This formulation rests on two major assumptions (quoted from GFP11): (i) tracer fluctuations are generated by local stirring of the large-scale tracer gradient, with the advection of tracer variance from upstream regions being weak, and (ii) the tracer gradient varies slowly over the distance L_{mix}.

The mixing length framework has widely been applied for the closure of geostrophic turbulence since it can link the eddy tracer transport to a downgradient flux in Eulerian form. Diffusivity k of generalized tracer φ (which approximately follows PV contours) due to isopycnal stirring is parameterized as

$$\overline{v'\varphi'} \;=\; -k\frac{\partial \varphi}{\partial y} \qquad (2),$$

where the overbars indicate temporal average in the isopycnal layer, the primes indicate deviations from those averages, and the tracer gradient is assumed to be meridional. v is meridional velocity so that the tracer flux is the covariance between tracer anomaly and cross-frontal velocity. Here, it is assumed *a priori* that tracer φ mixes purely along isopycnals. This assumption is equivalent to conditions that the mixing process is statistically steady, adiabatic, and solely caused by linear waves (e.g., Vallis, 2017). We may choose any passive tracer for φ if the tracer concentration represents the PV field, where its diffusion satisfies a requirement for the GM flux (Gent and McWilliams, 1990) mimicking baroclinic instability and the scalar coefficient of downgradient PV flux can express the skew component of diffusivity tensor.

One possible choice for L_{mix} is characteristic eddy scale (Klocker and Abernathey, 2014; Bates et al., 2014), which can be determined by the altimetric velocity field. Another possible choice is a rather empirical way of using hydrographic data. Emulating the arguments of Armi and Stommel (1983), GFP11 derived L_{mix} in the Southern Ocean from hydrographic variability, i.e.,

$$L_{\mathrm{mix}} = \frac{\sigma(\varphi)}{|\nabla \varphi|} \qquad (3).$$

Although they used isopycnal temperature for the conservative tracer φ, other candidates exist for the tracer variable (e.g., isopycnal spiciness and layer thickness). By the equations (1)–(3), the mixing efficiency follows as

$$\Gamma = \frac{\overline{v'\varphi'}}{\sigma(v)\ \sigma(\varphi)} \qquad (4),$$

that is identical to the correlation coefficient between v and φ. There are a wide range of estimates for Γ (0.01–0.4; Holloway and Kristmannsson, 1984; Visbeck et al., 1997; Karsten and Marshall, 2002) likely depending on the variety of

L_{mix} definitions. GFP11 noted that the only observational estimate $\Gamma = 0.16$ provided by Wunsch (1999) might be used for illustrating absolute values of k.

The hydrographic estimate of eddy diffusivity by GFP11 is broadly consistent with a more direct estimation via Lagrangian tracer dispersion numerically advected with altimetric velocity (Marshall, 2006; Sallée et al., 2011), generally falling into 500–3000 $\mathrm{m^2\ s^{-1}}$ within the ACC core and 2000–3500 $\mathrm{m^2\ s^{-1}}$ in its equatorward flank. The resulting map of diffusivity can be explained by the suppression theory deduced from weakly nonlinear wave–mean flow interaction (Ferrari and Nikurashin, 2010), interpreted as that jet-induced advection reduces eddy's continuous action for the same water mass and suppresses mixing length. The suppression of eddy stirring ceases in "leaky jets," likely associated with non-parallel shear flows and meanderings steered by the topography (GFP11; Sallée et al., 2011; Tamsitt et al., 2018). Klocker and Abernathey (2014) conducted numerical simulations to test the quantitativeness of the mixing length framework. They remarked that diffusivity could equivalently be estimated in a hypothetical unsuppressed mixing regime by either the eddy scale/tracer-based mixing length formulations if choosing =0.15 for the tracer-based mixing length, supporting the estimate of Wunsch (1999). These studies rationalize using the hydrographic variability method: the equations (1) and (3), and thus we apply them for quantifying eddy diffusion.

3. Data and methods

3.1 Satellite altimetry for $\mathbf{U}_{\mathrm{eddy}}$

An observational estimate of characteristic eddy velocity U_{eddy} can be given by altimetric velocity in the open ocean, while the satellite altimetry has previously been unavailable in the seasonal ice zone. Later, the advent of synthetic aperture interferometric radar altimeter enabled to measure sea ice freeboard remotely, and its application to dynamic ocean topography has recently been developed (Armitage et al., 2018; Mizobata et al., 2020). The present study adopts the monthly-reconstructed 0.2° grid dynamic ocean topography during 2011–2020 by Mizobata et al. (2020) to derive geostrophic velocities (Fig. 2). This dataset has an advantage over the product by Armitage et al. (2018) as its empirical orthogonal function filtering can remove spurious stripe patterns.

U_{eddy} is calculated as the standard deviation of altimetric flow speed (lower panel of Fig. 2). Its reliability is underpinned by the mooring measurements at 113°E (Pena-Molino et al., 2016), marking standard deviations of 0.04–0.06 $\mathrm{m\ s^{-1}}$ in zonal and meridional directions at the CDW depth (~500 dbar). The typical value of U_{eddy} is somewhat larger than the choice of FRE19 (0.017 $\mathrm{m\ s^{-1}}$), as they adopted the temporal mean velocity from the same mooring data. In principle, U_{eddy} is standard deviation of the cross-frontal velocity. However, in contrast to the ACC's mainstream, the flow field in the Antarctic margin is stagnant, and the mean flow directions are ambiguous (upper panel of Fig. 2). To bypass this problem, we simply define U_{eddy} as the root-mean-squared velocity, accounting for its good agreement with the direct flow measurement

(Pena-Molino et al., 2016).

Vertical variations of eddy velocity are neglected in this study. GFP11 treated this issue by applying the gravest empirical mode analysis to derive geostrophic shear. The gravest empirical mode scheme is very effective in the ACC domain, while it cannot be applied for the Antarctic margin as the dynamic topography does not descend poleward monotonically. Nevertheless, we consider that U_{eddy} adopted for CDW is acceptable because the vertical attenuation due to geostrophic shear is considerably small in the Antarctic margin by the quasi-barotropic flow structure (Pena-Molino et al., 2016; Mizobata et al., 2020; Yamazaki et al., 2020).

3.2 CTD profiles for $\mathbf{L}_{\mathrm{mix}}$

Mixing length L_{mix} is calculated from hydrographic variability by the equation (3). We assemble historical CTD profiles from World Ocean Database (https://www.ncei.noaa.gov/; for shipboard CTD), Argo Global Data Assembly Center (Argo, 2000), and Marine Mammals Exploring the Oceans Pole to Pole archive (https://www.meop.net/; Treasure et al., 2018). Data are extracted for December–March and 1990 onwards. After removing bad flagged data and fragmented profiles, 1-dbar Akima interpolation is performed for the CTD profiles. Surface data averaged within the neutral densities (Jacket and McDougall, 1997) are then constructed (Fig. 3), corresponding to CDW (defined as 28.0–28.1 kg m^{-3}) and Antarctic Surface Water (ASW; defined as 27.9–28.0 kg m^{-3}). The figures indicate that, in contrast to isopycnal temperature gradient of ASW stronger than CDW, isopycnal thickness gradient of CDW is generally stronger than ASW. Our focus is CDW, while a comparison to the ASW layer, with a larger number of data than the CDW layer, facilitates to check the layer dependency and the quantitativeness of k.

The previous studies adopted potential temperature and spiciness as the isopycnal tracer φ (GFP11; FRE19). However, it is unclear if these tracers yield diffusivity k conforming to volume transport expected by the downgradient PV diffusion (e.g., Marshall and Radko, 2003). Since the layer thickness is a possible candidate for the PV conservative variable (e.g., Vallis, 2017), the present study adopts both spiciness and layer thickness as the isopycnal tracer φ, and the diffusivities derived from the two variables are compared. Conservative Temperature, Absolute Salinity, and spiciness (at 0 dbar) are calculated using the Gibbs Sea Water Oceanographic Toolbox (http://www.teos-10.org/), and the layer thickness is derived from the pressure difference between the upper and lower isopycnal surfaces of each watermass.

Mapping surface data onto 0.2° grids is performed with the radius basis function interpolation (Yamazaki et al., 2020), which reproduces the best representative surface of noisy data nonparametrically in the least-squares sense. Grid data with less than 10 points inside a 75 km data radius are masked (gray area). Although the data coverage particularly reduces in 30–60°E, a sufficient number of data exist within the region of our interest (e.g., the continental slope

of 1,000–3,000 m isobaths). Correspondence among the 3,000 m isobath, –0.15 kg m^{-3} CDW spiciness, and 300 m CDW thickness (Fig. 3 right panels) guarantees fidelity of the interpolation. After calculating deviations of surface data from the gridded climatological field, root-mean-squared tracer variations $\sigma(\varphi)$ are derived in each grid from the deviation data within the 75 km radius. This procedure minimalizes artifacts in $\sigma(\varphi)$ due to the spatial variation of the tracer field within the data radius. The choice of the radius size is a trade-off between the data amount and the resolution, while our choice is comparable to the discussion by GFP11 that "about 5–10 stations per 100 km" is a reasonable baseline required for the L_{mix} calculation to capture the basic distribution patterns.

3.3 Validation of Mixing efficiency

One of the largest uncertainties of diffusivity k rests within the mixing efficiency Γ. Based on the equations (1) and (3), FRE19 indicated the along-slope variability of eddy condition in the East Antarctic margin via mapping standard deviation of isopycnal spiciness, while their formulation did not include Γ and spatially variable U_{eddy}, leaving some ambiguities for the absolute value of k. For a trial, we directly calculate Γ from the correlation coefficient between v and φ, using a 17-month mooring record across the ASC (in 113°E for 2010–2011; Pena-Molino et al., 2016). Vertical/meridional linear gridding (by 50 dbar for 200–1500 dbar and by 0.1 degrees for 65.5–61.5°S) is performed for hourly meridional velocity and temperature profiles to yield 1040 grids in total. During the 12 months (8761 steps), their correlation coefficient is calculated for each grid, assuming that the temperature variation is approximately coherent with the PV change and its gradient directs northward on average.

From the histogram of Γ, the mean value is estimated as 0.12 for down-gradient cases and 0.10 for all cases (Fig. 4). The up-gradient cases are possibly irrelevant to the climatological eddy condition since the downgradient velocity must direct southward by the mean temperature field (Fig. 3). Wunsch (1999) derived $\Gamma = 0.16$ from a global inventory of mooring records, broadly consistent with our estimates but larger by 30–40%. We must admit that 12 months is too short to determine eddy statistics with certainty (additional low-pass filtering may effectively cut off uninterested short-term variations, but such filtering possibly leads to underestimation). Based on the general agreement of the local value with the global estimate, the present study adopts the mixing efficiency $\Gamma = 0.16$ by Wunsch (1999) consistently with previous investigations (GFP11; Klocker and Abernathey, 2014). The validity of our choice is further discussed in Section 5.1.

4. Result

4.1 Mixing length

Standard deviation and normed gradient of isopycnal tracer φ for spiciness and layer thickness of each watermass are shown in Figs. 5 and 6, respectively. The large gradient of spiciness is concentrated near the ACC's southern boundary (SB; defined as the southernmost extent of 1.5 °C isotherms) in ASW (27.9–28.0

kg m^{-3}), while in CDW (28.0–28.1 kg m^{-3}), it emerges over the upper continental slope to the south (Fig. 5; top panels). The large standard deviation of spiciness broadly corresponds to its steep gradient. Relative to the spiciness gradient, the thickness gradient is likely homogeneous, and the coherence between the standard deviation and the gradient is less noticeable (Fig. 6). As in the spiciness, the sharp thickness gradient of CDW is found in the proximity of the SB, indicating a poleward volume flux represented by thickness diffusion (Yamazaki et al., 2020). Rounded patchy patterns appearing in the thickness-based diagnostics are likely associated with the distribution of standing eddies, while those signals are not visible in the spiciness-based values.

The lowermost panels in Figs. 5 and 6 present the mixing length L_{mix} derived from the equation (3). The patchy patterns in the thickness-based diagnostics do not emerge for L_{mix}. The spatial distributions of the spiciness/thickness-based L_{mix} are analoguous in terms of their meridional variations. These estimates are quantitatively consistent with the previous estimate by GFP11, where L_{mix} can exceed 150 km in the unsuppressed part of the ACC. Even though the spiciness/thickness-based diagnostics are highly dependent on the choice of isopycnal layer, the two L_{mix} estimates for CDW and ASW exhibit the highest value of ~150 km in the ACC domain and its suppression near the SB. These results suggest the quantitative robustness of the L_{mix} estimates. The spatial variation of L_{mix} is generally consistent with the jet-induced suppression theory (Ferrari and Nikurashin, 2010) as discussed in the following, while near-boundary turbulent suppression or "law of the wall" likely becomes more influential over the Antarctic margin than in the ACC domain.

The dependency of L_{mix} on the flow regime is detailed in Fig. 7. Estimates of L_{mix} are averaged in bins of mean flow speed and individually shown for the ACC frontal zones categorized by Orsi et al. (1995; see Figs. 1 and 2). The frontal zones refer to the dynamic topography data of Mizobata et al. (2020); the Subpolar Zone (south of SACCF-S): $<$ –1.85 m, the Southern Zone (from the SACCF-S to SACCF-N): –1.85 ~ –1.6 m, and the Antarctic Zone (from SACCF-N to PF): –1.6 ~ –1.0 m. Readers are advised to compare Fig. 7 with the result by GRP11 (their Fig. 10), which puts emphasis on the more energetic part of ACC to the north. In the Antarctic and Southern Zones, L_{mix} tends to decrease from 70–90 to 30–60 km as the flow speed increases from zero to 0.5 m s^{-1}, indicating suppressed mixing due to wave–mean flow interaction. In the Antarctic Zone, L_{mix} partly increases with the mean flow exceeding 0.5 m s^{-1}, corresponding to leaky jets in the lee of topographic features such as the Kerguelen Plateau (~80°E) and the Southeast Indian Ridge (~150°E; see Fig. 2). On the other hand, L_{mix} is not dependent of flow speed in the Subpolar Zone, ranging from 20 to 60 km. These results suggest that the jet-induced mixing suppression previously documented in the northern part of the ACC is less effective poleward. We posit that the mixing suppression in the Subpolar Zone is associated with the near-boundary turbulent suppression by the continental slope topography. We also confirmed that discussion for the L_{mix} dependency on the flow speed unchanged in case the inversion of suppression

factor (Ferrari and Nikurashin, 2010) is taken as the horizontal axis. In Fig. 7, inter-layer dependencies are unclear, accounting for the different data coverages of ASW and CDW (Fig. 3). Meanwhile, the thickness-based L_{mix} for ASW in the Subpolar Zone is exceptionally large for strong flows with relatively large standard errors. Its difference from the spiciness-based estimates is possibly due to the less distinctive gradient of thickness than spiciness in ASW (Figs. 5 and 6). It should be noted that the hydrographic variability method can yield L_{mix} and isopycnal diffusivity k quantitatively consistent with the previous estimates, while the choice of the isopycnal tracer φ occasionally affects the outcome and thus requires some rationale (as considered in the next section).

To monitor the transition of L_{mix}'s controlling factor towards the Antarctic margin, a histogram of L_{mix} is plotted on $\sigma(\varphi)$–$1/|\nabla\varphi|$ space (Fig. 8), in which all coordinates are normalized by their averages, the isolines of $L_{\mathrm{mix}} = 20$, 100 km are shown by white contours, and the averaged diagnostics for each layer/method are marked by plus. The poleward suppression of L_{mix} is readily observed by comparing the positions of population and plus among the frontal zones. In all presented layers and methods, modes and averages of L_{mix} are aligned with the $1/|\nabla\varphi|$ axis in the Antarctic Zone, and they migrate towards the $\sigma(\varphi)$ axis across the diagonal line as moving poleward. Significant learning drawn from this plot is that the inversed tracer gradient $1/|\nabla\varphi|$ becomes more influential poleward to the spatial variation of L_{mix} than $\sigma(\varphi)$ does (i.e., the variation of L_{mix} in the cross-isoline direction is hardly explained by $\sigma(\varphi)$ in the Subpolar Zone in contrast to the Antarctic and Southern Zones). This is because the poleward PV gradient becomes steeper (equivalently, the width of baroclinic zone becomes narrower) to the south, plausibly due to the continental slope topography. The topographic control of L_{mix} signifies a possibility to parameterize the eddy diffusivity using prescribed topographic information in an ocean model, as recently explored by idealized numerical simulations (Stewart and Thompson, 2016). We anticipate that, in the Subpolar Zone, L_{mix} and k can be predicted by the topographic gradient, and this idea will be assessed in the next section.

4.2 Isopycnal diffusivity

Based on the general agreement with the previous studies in the ACC domain, the diffusive parameters in the Antarctic margin are investigated more closely. Using the mixing length formulation of the equation (1), the isopycnal diffusivity k is calculated as the product of mixing efficiency Γ, eddy velocity U_{eddy}, and mixing length L_{mix}. Fig. 9 provides diffusivity maps for CDW diagnosed by spiciness and thickness, focusing on the Subpolar Zone. The climatological flow direction is represented by the mean dynamic topography overlaid, and contours characteristic to the subpolar circulation (–1.97 and –1.85 m) are highlighted in blue. The isopycnal diffusivity k typically ranges 100–500 $\mathrm{m^2\ s^{-1}}$ in the Subpolar Zone for both tracer variables, and k likely becomes small near the SB, which shapes the transition zone from ACC to ASC. The spatial variation of k within the Subpolar Zone seems attributable to the spatial variation of L_{mix} (Figs. 5

and 6) rather than U_{eddy} (Fig. 2) and thus to the PV gradient change (as seen in Fig. 8). To visualize the along-slope variability of k, local maps of thickness-based diffusivity are shown in Fig. 10 with the isopycnal CDW temperature. Importantly, diffusivity is likely higher where the onshore CDW intrusion occurs: 70°, 90°, 110°, and 120°E (these intrusion pathways are documented in Yamazaki et al., 2020). Additionally, enhanced diffusivity is observed in 140°E (Fig. 9), where intervals between ACC and ASC become narrow and clockwise subgyres are meridionally squeezed. The mechanism for this nontrivial correspondence between the eddy diffusion and the onshore CDW intrusion will be argumented in Section 5.4.

The spatial variation of k results from those of L_{mix} and U_{eddy}, and its functional dependency varies in space. Analogously to Fig. 8, a histogram of k in U_{eddy}–L_{mix} coordinates is plotted for each layer and method (Fig. 11). In any frontal zone, neither of L_{mix} and U_{eddy} is a dominant controlling factor as the population and the center of mass are located close to the diagonal line. Still, we may state that k is more dependent on L_{mix} than U_{eddy} in the Subpolar Zone, contrasting to the Southern and Antarctic Zones. The result supports the aforementioned idea that the spatial scale of tracer gradient can parametrize eddy diffusivity in the Antarctic margin via mixing length formulation. This idea is further tested by Fig. 12, in which k, L_{mix}, and the inversed topographic gradient within the Subpolar Zone are regressed onto the inversed tracer gradient $1/|\nabla\varphi|$, coordinated with nondimensionalized axes, and the scatters are colored by the altimetric mean velocity. Not surprisingly, significant correlations of k and L_{mix} with $1/|\nabla\varphi|$ are obtained (0.73 and 0.89 for spiciness; 0.81 and 0.92 for thickness, respectively). On the other hand, the correlation between the topographic and tracer gradients is insignificant for both tracers, implying that additional information is required to derive the climatological tracer gradient from the topographic data. Despite that controlling factors for the tracer gradient field remain veiled, the present result is encouraging since it allows us to predict eddy diffusion adequately if only we somehow determine the gradient of isopycnal tracers.

Compared to the spiciness-based estimation, the correlation of the thickness-based estimation with diffusivity is more statistically significant. The higher correlation of thickness implies that the thickness gradient better represents the PV gradient and the width of the baroclinic zone than the spiciness gradient does. This result seems quite reasonable provided that the ambient PV field is well approximated by the isopycnal layer thickness within the Subpolar Zone, where the flow condition is stagnant, and the relative vorticity likely becomes small. Predicated on these facts, we proceed to estimate the diffusive transport applying the thickness-based diffusivity to the isopycnal thickness field.

4.3 Volume and heat transport

Assuming that the isopycnal thickness simply diffuses downgradient in a GM-flux manner, we can estimate diffusive volume flux of CDW (Fig. 13). Bolus transport ψ is calculated as

$$\psi \; = \; -k_H \nabla \mathrm{H} \qquad (5),$$

where H and k_H are the isopycnal layer thickness and the thickness-based diffusivity, respectively. This is equivalent to the layer-integrated bolus velocity (in $m^2\ s^{-1}$), and its horizontal integration gives a unit of transport. The zonal eddy transport likely directs downstream in the lee of topography and upstream in the other area (middle panel), indicative of the internal form stress balance within the ACC (Marshall et al., 2017). As a result of the thickness gradient, the volume transport generally directs shoreward in the Subpolar Zone, as represented by the transport vector direction and its meridional component (lower panel). We can observe the poleward CDW transport continuously extending from the eastern flank of the Kerguelen Plateau, where isopycnal eddies are favorably generated, to the continental margin. Along-slope variation of the meridional eddy transport is not so pronounced as k (Fig. 9), and the most significant poleward CDW transport is obtained around 140°E. This is because the magnitude of transport is $|\psi| = \Gamma U_{\mathrm{eddy}} \sigma(H)$ by the equation (3) and is not proportional to the inversed thickness gradient (whether CDW flux becomes uniquely proportional to U_{eddy} is unclear even in zonally-symmetric configuration regarding possible variability of mixing efficiency; e.g., Stewart and Thompson, 2016). Partially northward eddy transport along the continental slope (e.g., around 70°E) likely reflects the multiple-cored ASC over the gentle continental slope, which has emerged in previous literature (Meijers et al., 2010; Stewart and Thompson, 2016).

The meridional component of ψ is zonally integrated to derive the cross-slope fluxes of volume and heat (Fig. 14; over the 1000–3000 m isobaths). Standard errors associated with the cross-slope variation are shaded, within which heat flux change due to the along-slope temperature variation safely falls. The gross onshore CDW transport is 0.39/0.12 Sv ($= m^3\ s^{-1}$) in the eastern/western Indian sectors (divided by the Princess Elizabeth Trough ~90°E), respectively, translated to the onshore heat fluxes of 3.6/1.2 TW. The interbasin contrast in thermal forcing seems consistent with the stratification regimes inshore, represented by warm Totten Ice Shelf and cold Amery Ice Shelf (Silvano et al., 2016).

Offshore transport of ASW to the west of 130°E is 0.15 Sv, balancing with ~40 % onshore volume flux by CDW. On the contrary, ASW eastward of 130°E is transported to the pole, and its contribution to the onshore heat flux (~0.4 TW) might not be negligible. As discussed in Section 5.2, these estimates are quantitatively consistent with the coastal heat sink due to sea ice formation and glacial melting.

5. Discussion

5.1 Diffusivity estimation

The present study is fundamentally based on the assumption that the mixing

length framework is valid to the extent of our interest. One of the necessary conditions for the formulation (see Section 2) is a scale separation between L_{mix} and the spatial variation of $\nabla\varphi$. We estimated the typical value of L_{mix} to be 20–60 km in the Subpolar Zone (Fig. 7). $\nabla\varphi$ likely varies in the cross-slope direction by a scale comparable to or larger than the slope width (~100 km for the 1,000–3,000 m interval), so it is possible to regard this condition as holding in the Antarctic margin. The other necessary condition for L_{mix} estimation is that tracer fluctuations must reflect local eddy stirring rather than tracer anomalies advected from upstream. This condition also likely holds in the Antarctic margin, given the weaker nonlinearity than the ACC's mainstream (Fig. 3).

No significant difference is found between the thickness-based and spiciness-based L_{mix} (Figs. 5 and 6). To our knowledge, the present study is the first example to demonstrate that the two choices of tracer yield very similar L_{mix} estimates. This infers quantitativeness of a series of previous estimates, in which isopycnal tracers not necessarily dependent on PV have been adopted (GFP11; FRE19; Armi and Stommel, 1983). Meanwhile, a small but noticeable difference between the spiciness/thickness-based estimations is obtained; e.g., the large thickness-based (spiciness-based) k in 70°E (110°E) seems weak by the counterpart method. The flow dependency of L_{mix} also likely varies by choice of tracer (Fig. 7). These subtle contrasts generally pertain to the local difference in the tracer gradient, as the large diffusivities likely result from the weak tracer gradient. We found that the thickness gradient better represents the variations of L_{mix} and k than the spiciness gradient (Fig. 12) attributable to the PV-conservative nature of isopycnal thickness. The thickness-based L_{mix} and k rationalize the calculation of thickness-diffusive transport, accounting for the residual overturning theory (Marshall and Radko, 2003).

Although the estimated diffusivity of 100–500 $\mathrm{m^2\ s^{-1}}$ is significantly smaller than the along-slope estimation of 950 ± 400 $\mathrm{m^2\ s^{-1}}$ presented by FRE19 (based on spiciness variability), their estimate implicitly assumed the mixing efficiency Γ to be unity (far exceeding its previous estimates; 0.01–0.4) and hence seems incompatible as an absolute diffusivity estimation. In case $\Gamma = 0.16$ by Wunsch (1999) is consistently applied for their values, the isopycnal diffusivity of 90–220 $\mathrm{m^2\ s^{-1}}$ is obtained from their result, rather smaller k than our estimate. Further, our estimation is quite consistent with previous studies in the ACC's mainstream, typically ranging for 500–2000 $\mathrm{m^2\ s^{-1}}$ (Marshall et al., 2006) and 1500–3000 $\mathrm{m^2\ s^{-1}}$ (Sallée et al., 2011) with a poleward decrease.

To investigate the meridional overturning circulation across the ASC jets in zonally symmetric configuration, Stewart and Thompson (2016) conducted idealized numerical experiments. They demonstrated that L_{mix} scaled by the slope width accurately predicts the simulated onshore flux of CDW ($\mathrm{R^2} = 0.89$). However, we found that L_{mix} is significantly correlated with the thickness gradient but not with the topographic gradient (Fig. 12). This dissociation with the topographic slope scale may be interpreted because of thickness control by the

surface layer, expected from shelf water export in the clockwise subgyres (Yamazaki et al., 2020). We assume that the thickness field itself is strongly connected to the zonally asymmetric structures of circulation and topography (see Section 5.4).

The inaccessible but most uncertain part of our estimate is the spatial variability of mixing efficiency. Visbeck et al. (1997) argumented that eddy transfer coefficient, which determines the proportionality of diffusivity to the horizontal/vertical stratification and the width of baroclinic zone, is a universal constant (equal to 0.015) regardless of flow regime. Mixing efficiency is different from this coefficient by its formulation, but they are possibly associated with each other. Validity of $\Gamma = 0.16$ is dependent on, let alone mooring data analyzed in Section 3.3, discussion by Klocker and Abernathey (2014) that $\Gamma = 0.15$ is suitable for the tracer-based mixing length calculation to be consistent with diffusivity by altimetric eddy scale. Examination for its universality is a future task and requires a utility of numerical models. Although the spatial variation of Γ can alter the correspondence between the enhanced diffusivity and the CDW intrusions (Fig. 10), the presented result leastwise suggests that mixing length is large where CDW intrudes shoreward. Furthermore, it is presumable that its spatial variation is negligible when considering a basin-wide transport as in the next section.

5.2 Coastal transport and heat budgets

The estimated onshore heat/volume flux (Fig. 14) is quantitatively consistent with the previously reported coastal budgets. As for integration within the eastern Indian sector (90–160°E), the annually-cumulative sea ice production is 520 ± 75 km^3 (Tamura et al., 2016; a sum of Shackleton, Vincennes, Dalton, Dibble, and Mertz Polynyas), being translated to heat loss of 4.2–5.6 TW. The integrated ice shelf basal melt rate is 198 ± 39 Gt yr^{-1} (Rignot et al., 2013; a sum of Mertz, Dibble, Holmes, Moscow Univ., Totten, Vincennes, Conger, Tracy, and Shackleton Ice Shelves), being translated to 1.7–2.5 TW. Therefore, the CDW heat flux of 3.2–3.9 TW (within the 28.0–28.1 kg m^{-3} neutral density) compensates for nearly half of the cryospheric heat sink and thus is a major source of heat for the Antarctic coasts. Missing source of heat (~3 TW) and offshore heat advection is likely balanced by solar heating (~5 TW within 100 km from the coastline of 90–160°E; Tamura et al., 2011) and the partial onshore intrusion of ASW (to the east of 130°E; Fig. 14).

As connectivity of the on-shelf current over the Antarctic coastline is likely weak in the Indian sector (Dawson et al., 2021), the volume imbalance between CDW and ASW implies the local exporting volume of Antarctic Bottom Water. In this sense, the partial intrusion of ASW to the east (Fig. 14) is likely consistent with the intensive bottom water formation in the Adelie/Mertz region (Williams et al., 2010), which might be ~0.3 Sv on the annual mean basis (from a numerical simulation by Kusahara et al., 2017). To the west of 130°E, the ASW export only balances with ~40% of the CDW influx, so that the remaining volume (~0.2 Sv) may be attributable to the bottom water export in Vincennes Bay (Kitade et al.,

2014), Cape Darnley (Ohshima et al., 2013), and the rest of minor formation sites. The CDW volume compensation for the bottom water export can be numerically simulated over the circumpolar domain (Morrison et al., 2020). This study provides the first observational implication for the phenomenon with the quantitative estimation of the coastal heat/volume budgets.

Results by Stewart and Thompson (2016) indicate a possibility to underestimate the onshore heat flux derived from the mixing length formulation solely based on the thickness-diffusive CDW flux (likely corresponding to "eddy advection"), as the isopycnal "eddy stirring" can also contribute to the heat flux without transporting water volume, especially near the shelf break. The remarkable heat budget closure pertains to the situation that, compared to the eddy advection, the eddy stirring and tidal mixing are not dominant over the targeted slope (1000–3000 m; Fig. 14), as indicated by a realistic simulation (Stewart et al., 2018), and most of the heat flux explained by eddy advection over the isobaths subsequently reaches the Antarctic coast beyond the shelf break. On the other hand, the poleward CDW transport by the cross-slope geostrophic current (measured in seaward of the 3000 m isobath; Mizobata et al., 2020) might be confined to the lower continental slope, consistent with the numerical model (Stewart et al., 2018) and the weak shoreward advection of profiling floats (Yamazaki et al., 2020).

5.3 Diapycnal fluxes

The divergence of ψ is also calculated to evaluate the diapycnal flux in the Antarctic margin (Fig. 15, top panel). It can be decomposed into the thickness squeezing term and the symmetric diffusion term:

$$\nabla \cdot \psi \; = \; -\nabla k_H \cdot \nabla H - \; k_H \nabla^2 H \qquad (6),$$

and both are explicitly computable (Fig. 15; middle and bottom panels, respectively). Since ∇k_H likely reflects the spatial variation of k_H at the upper surface (28.00 kg m^{-3}) rather than a tranquil deeper layer, divergent (convergent) thickness squeezing $-\nabla k_H \cdot \nabla H$ can be interpreted as upward (downward) diapycnal flux through the upper surface (left panel of Fig. 15). Likewise, since ∇H likely reflects its variation at the lower surface (28.10 kg m^{-3}) rather than undulation of shallower isopycnals, divergent (convergent) symmetric diffusion $- \; k_H \nabla^2 H$ can be interpreted as downward (upward) diapycnal flux through the lower surface. These ideas are translated to the diapycnal velocity over the Subpolar Zone; the net convergence of 1.0 ± 11 µm s^{-1} for the CDW density (28.00–28.10 kg m^{-3}) is decomposed into upward diapycnal fluxes of 1.8 ± 16 µm s^{-1} (at the upper surface) and 2.8 ± 21 µm s^{-1} (at the lower surface). Even though the spatial variability is quite large, these averaged values are very comparable to Ekman upwelling of ~2 µm s^{-1} typical in the Antarctic margin (Liang et al., 2017). This agreement might further underpin the quantitativeness of our estimation.

The net upward diapycnal flux due to the symmetric diffusion term $- \; k_H \nabla^2 H$ may be a manifestation of the convex curvature of the lower isopycnal (Fig. 15,

right panel). On the other hand, the net upward diapycnal flux by the thickness squeezing term $-\nabla k_H \cdot \nabla H$ can be interpreted due to the seaward gradient of k_H. It is attributable to the gradual inclination of upper isopycnal from the SB to the continental shelf, since k_H is highly correlated with the magnitude of thickness gradient (Fig. 12). This situation is checked by the fact that $-\nabla k_H \cdot \nabla H$ tends to be positive to the south of SB (Fig. 15, middle panel). These arguments imply that, even though the isopycnal gradient is well correlated with that of topography (Yamazaki et al., 2020), the spatial distribution of CDW thickness is not simply determined by the structure of topography but also by the interface between CDW and ASW, so their discordance encountered in Fig. 12 appears to be reasonable.

The divergence of isopycnal eddy advection indicates the net upward diapycnal fluxes through the upper and lower surfaces of the CDW layer (Fig. 15, right panel). The net diapycnal upwelling seems consistent with the kinematic analysis of the layer thickness, in which both thickness squeezing and symmetric diffusion terms are controlled by thickness Laplacian as the isopycnal diffusivity k is highly dependent on the inversed thickness gradient (Fig. 12). These diapycnal fluxes are likely significant for modifying CDW along the isopycnal pathway over the continental slope, controlling the property of modified CDW inshore. Furthermore, the local diapycnal upwelling can explain why isopycnal/temperature surfaces tend to be shallow where the CDW intrusion occurs (Yamazaki et al., 2020; see their Figs. 8 and 10). Its vertical position relative to the topography is critical to whether the CDW isopycnal is bridged to the continental shelf. On the other hand, offshore advection of ASW might also play a crucial role in the vertical adjustment of CDW, and thus the effect of diapycnal flux needs to be further evidenced. Even though a basin-scale upwelling is naturally expected from the divergent wind stress in the Subpolar Zone, the presented result is valuable as an observational estimate of the climatological diapycnal flux, possibly demonstrating its spatial variation associated with the circulation and topography.

5.4 Circulation and eddy fluxes

We found that L_{mix} and k are likely large where the onshore CDW intrusion is localized (Fig. 10), indicating that the onshore CDW intrusion is achieved by the cross-slope eddy advection. Upon this result, we can speculate how the CDW intrusion is established. First, the recirculating gyres steered by the barotropic PV and horizontal shear between the ACC and ASC determine the location of shoreward intrusion. Offshore CDW then approaches the continental slope advected by a quasi-barotropic flow branched from the ACC. Due to the ambient PV constraint, the mean flow cannot reach the upper slope (inshore of ~3000 m); instead, this encroachment steepens the gradient of CDW isopycnal. The steepened isopycnal locally causes baroclinic instability, and, subsequently, the generated eddies facilitate the onshore eddy advection.

The explanation in the previous paragraph should be rationalized along with two facts: (i) the magnitude of ψ (i.e., $\Gamma U_{\mathrm{eddy}} \sigma(H)$) is independent of ∇H and

(ii) L_{mix} and k are "inversely" proportional to ∇H by the equations (1) and (3). The latter suggests that the inversed thickness gradient is associated with isopycnal tracer fluctuations and U_{eddy} (in short, "ability to mix") rather than the geostrophic stability. This infers that a steep thickness gradient is associated with the strong mean flow and likely prevents cross-frontal eddy transport, as schematized in Fig. 16. On the other hand, the former infers that the spatial variation of eddy transport ψ reflects that of tracer fluctuations and U_{eddy} rather than the ∇H field. Since U_{eddy} likely has a minor effect on the spatial variation (accounting for Fig. 11), we may interpret the large shoreward eddy transport in the intrusion sites as manifesting a large $\sigma(H)$ and L_{mix}, as suggested by FRE19. The baroclinic eddy generation accompanied by the cross-slope CDW flux is expected to occur intermittently, with a gentle thickness gradient on average. In contrast, the sharp thickness gradient is likely associated with a baroclinically stable part of the ASC, hence unintrusive (Fig. 16). This situation may be noticed by comparing the CDW thickness and isotherm (Yamazaki et al., 2020; their Fig. 10), where thicker CDW and its smaller gradient can be observed in the intrusion sites. The situation illustrated in Fig. 16 implicates that the ASC behaves as a barrier to the onshore CDW intrusion. The dynamical driver governing the thickness field remains unknown, yet we posit that ASW's property, as well as topographic steering, plays an indispensable role.

6. Conclusion

To investigate the controlling factor of onshore CDW intrusion across the Antarctic continental slope, the present study conducted an extensive analysis of hydrographic measurements and the satellite altimetry data taking advantage of the mixing length formulation. The spiciness/thickness-based estimations yielded qualitatively similar results, supporting the fidelity of the mixing length estimates previously made using hydrographic variability. The same analysis is applied for ASW, and its mixing length close to CDW was obtained. Over the ACC domain (Antarctic and Southern Zones), a general agreement with the mixing suppression theory and its exception in the lee of the topography is found, as previously reported (GFP11). In contrast, no mixing length's dependency on mean flow is obtained in the Subpolar Zone, reflecting a stagnant flow regime in the Antarctic margin. Eddy diffusion is likely enhanced where the CDW intrusion is localized by the recirculating gyres, which are steered by the barotropic PV (i.e., topography). This correspondence is primarily attributable to the spatial variation of diffusivity controlled by the isopycnal thickness gradient, and the gentle thickness gradient allows for ease of isopycnal mixing. Volume transport is estimated in a GM-flux manner, and it is shown that thickness-diffusive onshore heat flux over the continental slope is quantitatively consistent with cryospheric heat sinks (sea ice formation and ice shelf basal melt), suggesting that the isopycnal eddy advection is the main factor of the onshore CDW intrusion. Upward diapycnal fluxes across the CDW isopycnals are indicated by kinematic analysis of eddy flux divergence, in which thickness squeezing and symmetric diffusion terms cause upward fluxes in the

upper and lower surfaces, respectively. The estimated diapycnal flux is broadly consistent with upwelling predicted by cyclonic wind stress, further supporting our quantification. Predicated on these findings, the mechanism of eddy flux localization is speculated, and the controlling factors of the onshore CDW intrusion are illustrated in Fig. 16. Our findings may break new ground on the Southern Ocean dynamics, in which a connection between the meridional overturning circulation and the coastal buoyancy budget has been hypothesized (e.g., Snow et al., 2016; Morrison et al., 2020).

As a concluding remark, we underscore that the isopycnal thickness field is essential for determining the eddy fluxes in the Antarctic margin. The presented results facilitate a possibility to predict the eddy diffusivity by solely determining the layer thickness. This idea might be valuable for simulating CDW transport in global climate models, where subgrid effects of eddy fluxes need to be parameterized. Detailed reproduction of eddy flux is substantial for the multidecadal variability of onshore CDW flux (Yamazaki et al., 2021) and is inevitable for climate projection with higher credibility.

Acknowledgments

We are grateful to Argo Program and MEOP project for significant deployment efforts in Southern Ocean and successive QC processes. This study was financially supported by JSPS KAKENHI Grant Numbers 21H04918. We thank A. Kubokawa, and Y. Yoshikawa for their valuable comments and B. Pena-Molino for providing the I9S mooring records. The authors declare no competing interest.

Open Research

All hydrographic data is available to public as detailed in Section 3.2. Dynamic topography data can be downloaded from (TO BE FILLED). Python codes used in the present study (data processing, analysis, and figure creation) are available from the corresponding author upon request.

References

Abernathey, R. P., Cerovecki, I., Holland, P. R., Newsom, E., Mazloff, M., & Talley, L. D. (2016). Water-mass transformation by sea ice in the upper branch of the Southern Ocean overturning. *Nature Geoscience*, *9*(8), 596–601. https://doi.org/10.1038/ngeo2749

Argo (2000). Argo float data and metadata from Global Data Assembly Centre (Argo GDAC). SEANOE. https://doi.org/10.17882/42182

Armi, L., & Stommel, H. (1983). Four Views of a Portion of the North Atlantic Subtropical Gyre. *Journal of Physical Oceanography*, *13*(5), 828–857. https://doi.org/10.1175/1520-0485(1983)013<0828:FVOAPO>2.0.CO;2

Bates, M., Tulloch, R., Marshall, J., & Ferrari, R. (2014). Rationalizing the spatial distribution of mesoscale eddy diffusivity in terms of mix-

ing length theory. *Journal of Physical Oceanography*, *44*(6), 1523–1540. https://doi.org/10.1175/JPO-D-13-0130.1

Beckmann, A., & Pereira, A. F. (2003). Lateral tidal mixing in the Antarctic marginal seas. *Ocean Dynamics*, *53*(1), 21–26. https://doi.org/10.1007/s10236-002-0020-9

Cessi, P. (2019). The global overturning circulation. *Annual Review of Marine Science*, *11*, 249–270. https://doi.org/10.1146/annurev-marine-010318-095241

Dawson, H., Morrison, A., Tamsitt, V., & England, M. (2021). Pathways and timescales of connectivity around the Antarctic continental shelf. In *EGU General Assembly 2021* (p. 14011). https://doi.org/10.5194/egusphere-egu21-14011

Ferrari, R., & Nikurashin, M. (2010). Suppression of eddy diffusivity across jets in the Southern Ocean. *Journal of Physical Oceanography*, *40*(7), 1501–1519. https://doi.org/10.1175/2010JPO4278.1

Foppert, A., Rintoul, S. R., & England, M. H. (2019). Along-Slope Variability of Cross-Slope Eddy Transport in East Antarctica. *Geophysical Research Letters*, *46*(14), 8224–8233. https://doi.org/10.1029/2019GL082999

Gent, P. R., & Mcwilliams, J. C. (1990). Isopycnal Mixing in Ocean Circulation Models. *Journal of Physical Oceanography*. https://doi.org/10.1175/1520-0485(1990)020<0150:imiocm>2.0.co;2

Hirano, D., Mizobata, K., Sasaki, H., Murase, H., Tamura, T., & Aoki, S. (2021). Poleward eddy-induced warm water transport across a shelf break off Totten Ice Shelf, East Antarctica. *Communications Earth & Environment*, *2*(1). https://doi.org/10.1038/s43247-021-00217-4

Hogg, A. M. C., & Blundell, J. R. (2006). Interdecadal variability of the Southern Ocean. *Journal of Physical Oceanography*, *36*(8), 1626–1645. https://doi.org/10.1175/JPO2934.1

Holloway, G., & Kristmannsson, S. S. (1984). Stirring and transport of tracer fields by geostrophic turbulence. *Journal of Fluid Mechanics*, *141*, 27–50. https://doi.org/10.1017/S0022112084000720

Jackett, D. R., & Mcdougall, T. J. (1997). A neutral density variable for the world's oceans. *Journal of Physical Oceanography*, *27*(2), 237–263. https://doi.org/10.1175/1520-0485(1997)027<0237:ANDVFT>2.0.CO;2

Jenkins, A., Dutrieux, P., Jacobs, S., Steig, E. J., Gudmundsson, G. H., Smith, J., & Heywood, K. J. (2016). Decadal ocean forcing and Antarctic ice sheet response: Lessons from the Amundsen Sea. *Oceanography*, *29*(4), 106–117. https://doi.org/10.5670/oceanog.2016.103

Karsten, R. H., & Marshall, J. (2002). Constructing the residual circulation of the ACC from observations. *Journal of Physical Oceanography*, *32*(12), 3315–3327. https://doi.org/10.1175/1520-0485(2002)032<3315:CTRCOT>2.0.CO;2

Kitade, Y., Shimada, K., Tamura, T., Williams, G. D., Aoki, S., Fukamachi, Y., et al. (2014). Antarctic bottom water production from the Vincennes Bay Polynya, East Antarctica. *Geophysical Research Letters*, *41*(10), 3528–3534. https://doi.org/10.1002/2014GL059971

Klocker, A., & Abernathey, R. (2014). Global patterns of mesoscale eddy properties and diffusivities. *Journal of Physical Oceanography*, *44*(3), 1030–1046. https://doi.org/10.1175/JPO-D-13-0159.1

Kunze, E., Firing, E., Hummon, J. M., Chereskin, T. K., & Thurnherr, A. M. (2006). Global abyssal mixing inferred from lowered ADCP shear and CTD strain profiles. *Journal of Physical Oceanography*, *36*(8), 1553–1576. https://doi.org/10.1175/JPO2926.1

Kusahara, K., Hasumi, H., Fraser, A. D., Aoki, S., Shimada, K., Williams, G. D., et al. (2017). Modeling ocean-cryosphere interactions off Adélie and George V Land, East Antarctica. *Journal of Climate*, *30*(1), 163–188. https://doi.org/10.1175/JCLI-D-15-0808.1

LaCasce, J. H., & Bower, A. (2000). Relative dispersion in the subsurface North Atlantic. *Journal of Marine Research*, *58*(6), 863–894. https://doi.org/10.1357/002224000763485737

Liang, X., Spall, M., & Wunsch, C. (2017). Global Ocean Vertical Velocity From a Dynamically Consistent Ocean State Estimate. *Journal of Geophysical Research: Oceans*, *122*(10), 8208–8224. https://doi.org/10.1002/2017JC012985

Marshall, D. P., Ambaum, M. H. P., Maddison, J. R., Munday, D. R., & Novak, L. (2017). Eddy saturation and frictional control of the Antarctic Circumpolar Current. *Geophysical Research Letters*, *44*(1), 286–292. https://doi.org/10.1002/2016GL071702

Marshall, J., & Radko, T. (2003). Residual-mean solutions for the Antarctic Circumpolar Current and its associated overturning circulation. *Journal of Physical Oceanography*, *33*(11), 2341–2354. https://doi.org/10.1175/1520-0485(2003)033<2341:RSFTAC>2.0.CO;2

Marshall, J., Shuckburgh, E., Jones, H., & Hill, C. (2006). Estimates and implications of surface eddy diffusivity in the Southern Ocean derived from tracer transport. *Journal of Physical Oceanography*, *36*(9), 1806–1821. https://doi.org/10.1175/JPO2949.1

Mckee, D. C., Martinson, D. G., & Schofield, O. (2019). Origin and attenuation of mesoscale structure in Circumpolar Deep Water intrusions to an Antarctic shelf. *Journal of Physical Oceanography*, *49*(5), 1293–1318. https://doi.org/10.1175/JPO-D-18-0133.1

Meijers, A. J. S., Klocker, A., Bindoff, N. L., Williams, G. D., & Marsland, S. J. (2010). The circulation and water masses of the Antarctic shelf and continental slope between 30 and 80°E. *Deep-Sea Research Part II: Topical Studies in Oceanography*, *57*(9–10), 723–737. https://doi.org/10.1016/j.dsr2.2009.04.019

Mizobata, K., Shimada, K., Aoki, S., & Kitade, Y. (2020). The Cyclonic Eddy Train in the Indian Ocean Sector of the Southern Ocean as Revealed by Satellite Radar Altimeters and In Situ Measurements. *Journal of Geophysical Research: Oceans*, *125*(6). https://doi.org/10.1029/2019JC015994

Morrison, A. K., McC. Hogg, A., England, M. H., & Spence, P. (2020). Warm Circumpolar Deep Water transport toward Antarctica driven by local dense water export in canyons. *Science Advances*, *6*(18), 1–10. https://doi.org/10.1126/sciadv.aav2516

Naveira Garabato, A. C., Ferrari, R., & Polzin, K. L. (2011). Eddy stirring in the Southern Ocean. *Journal of Geophysical Research: Oceans*, *116*(9), 1–29. https://doi.org/10.1029/2010JC006818

Ohshima, K. I., Fukamachi, Y., Williams, G. D., Nihashi, S., Roquet, F., Kitade, Y., et al. (2013). Antarctic Bottom Water production by intense sea-ice formation in the Cape Darnley polynya. *Nature Geoscience*, *6*(3), 235–240. https://doi.org/10.1038/ngeo1738

Orsi, A. H., Whitworth, T., & Nowlin, W. D. (1995). On the meridional extent and fronts of the Antarctic Circumpolar Current. *Deep-Sea Research Part I*, *42*(5), 641–673. https://doi.org/10.1016/0967-0637(95)00021-W

Pauthenet, E., Sallée, J. B., Schmidtko, S., & Nerini, D. (2021). Seasonal variation of the antarctic slope front occurrence and position estimated from an interpolated hydrographic climatology. *Journal of Physical Oceanography*, *51*(5), 1539–1557. https://doi.org/10.1175/JPO-D-20-0186.1

Peña-Molino, B., McCartney, M. S., & Rintoul, S. R. (2016). Direct observations of the Antarctic Slope Current transport at 113°E. *Journal of Geophysical Research: Oceans*, *121*(10), 7390–7407. https://doi.org/10.1002/2015JC011594

Rignot, E., Jacobs, S., Mouginot, J., & Scheuchl, B. (2013). Ice-shelf melting around Antarctica. *Science*, *341*(6143), 266–270. https://doi.org/10.1126/science.1235798

Sallée, J. B., Speer, K., & Rintoul, S. R. (2011). Mean-flow and topographic control on surface eddy-mixing in the Southern Ocean. *Journal of Marine Research*, *69*(4–6), 753–777. https://doi.org/10.1357/002224011799849408

Shimada, K., Aoki, S., & Ohshima, K. I. (2017). Creation of a gridded dataset for the southern ocean with a topographic constraint scheme. *Journal of Atmospheric and Oceanic Technology*, *34*(3), 511–532. https://doi.org/10.1175/JTECH-D-16-0075.1

Silvano, A., Rintoul, S. R., & Herraiz-Borreguero, L. (2016). Ocean-ice shelf interaction in East Antarctica. *Oceanography*, *29*(4), 130–143. https://doi.org/10.5670/oceanog.2016.105

Snow, K., Hogg, A. M., Sloyan, B. M., & Downes, S. M. (2016). Sensitivity of Antarctic Bottom Water to changes in surface buoyancy fluxes. *Journal of Climate*, *29*(1), 313–330. https://doi.org/10.1175/JCLI-D-15-0467.1

Spence, P., Holmes, R. M., Hogg, A. M. C., Griffies, S. M., Stewart, K. D., & England, M. H. (2017). Localized rapid warming of West Antarctic subsurface waters by remote winds. *Nature Climate Change*, *7*(8), 595–603. https://doi.org/10.1038/NCLIMATE3335

Stewart, A. L., Klocker, A., & Menemenlis, D. (2018). Circum-Antarctic Shoreward Heat Transport Derived From an Eddy- and Tide-Resolving Simulation. *Geophysical Research Letters*, *45*(2), 834–845. https://doi.org/10.1002/2017GL075677

Stewart, A. L., Klocker, A., & Menemenlis, D. (2019). Acceleration and overturning of the antarctic slope current by winds, eddies, and tides. *Journal of Physical Oceanography*, *49*(8), 2043–2074. https://doi.org/10.1175/JPO-D-18-0221.1

Stewart, A. L., & Thompson, A. F. (2013). Connecting antarctic cross-slope exchange with southern ocean overturning. *Journal of Physical Oceanography*, *43*(7), 1453–1471. https://doi.org/10.1175/JPO-D-12-0205.1

Stewart, A. L., & Thompson, A. F. (2016). Eddy generation and jet formation via dense water outflows across the Antarctic continental slope. *Journal of Physical Oceanography*, *46*(12), 3729–3750. https://doi.org/10.1175/JPO-D-16-0145.1

Tamsitt, V., Drake, H. F., Morrison, A. K., Talley, L. D., Dufour, C. O., Gray, A. R., et al. (2017). Spiraling pathways of global deep waters to the surface of the Southern Ocean. *Nature Communications*, *8*(1), 172. https://doi.org/10.1038/s41467-017-00197-0

Tamura, T., Ohshima, K. I., Fraser, A. D., & Williams, G. D. (2016). Sea ice production variability in Antarctic coastal polynyas. *Journal of Geophysical Research: Oceans*, *121*(5), 2967–2979. https://doi.org/10.1002/2015JC011537

Tamura, T., Ohshima, K. I., Nihashi, S., & Hasumi, H. (2011). Estimation of surface heat/salt fluxes associated with sea ice growth/melt in the Southern Ocean. *Scientific Online Letters on the Atmosphere*, *7*(1), 17–20. https://doi.org/10.2151/sola.2011-005

Taylor, G. I. (1922). Diffusion by Continuous Movements. *Proceedings of the London Mathematical Society*, *s2-20*(1), 196–212. https://doi.org/10.1112/plms/s2-20.1.196

Thompson, A. F., Heywood, K. J., Schmidtko, S., & Stewart, A. L. (2014). Eddy transport as a key component of the Antarctic overturning circulation. *Nature Geoscience*, *7*(12), 879–884. https://doi.org/10.1038/ngeo2289

Thompson, A. F., Speer, K. G., & Schulze Chretien, L. M. (2020). Genesis of the Antarctic Slope Current in West Antarctica. *Geophysical Research Letters*, *47*(16). https://doi.org/10.1029/2020GL087802

Thompson, A. F., Stewart, A. L., Spence, P., & Heywood, K. J. (2018). The Antarctic Slope Current in a Changing Climate. *Reviews of Geophysics*, *56*(4),

741–770. https://doi.org/10.1029/2018RG000624

Treasure, A. M., Roquet, F., Ansorge, I. J., Bester, M. ., Boehme, L., Bornemann, H., et al. (2017). Marine Mammals Exploring the Oceans Pole to Pole. *Oceanography*, *30*(2), 132–138.

Vallis, G. K. (2017). *Atmospheric and Oceanic Fluid Dynamics*. Cambridge: Cambridge University Press. https://doi.org/10.1017/9781107588417

Visbeck, M., Marshall, J., Haine, T., & Spall, M. (1997). Specification of Eddy Transfer Coefficients in Coarse-Resolution Ocean Circulation Models*. *Journal of Physical Oceanography*, *27*(3), 381–402. https://doi.org/10.1175/1520-0485(1997)027<0381:SOETCI>2.0.CO;2

Williams, G. D., Aoki, S., Jacobs, S. S., Rintoul, S. R., Tamura, T., & Bindoff, N. L. (2010). Antarctic bottom water from the adélie and George v Land Coast, East Antarctica (140-149°E). *Journal of Geophysical Research: Oceans*, *115*(4), C04027. https://doi.org/10.1029/2009JC005812

Wunsch, C. (1999). Where do ocean eddy heat fluxes matter? *Journal of Geophysical Research: Oceans*, *104*(C6), 13235–13249. https://doi.org/10.1029/1999jc900062

Yamazaki, K., Aoki, S., Katsumata, K., Hirano, D., & Nakayama, Y. (2021). Multidecadal poleward shift of the southern boundary of the Antarctic Circumpolar Current off East Antarctica. *Science Advances*, *7*(24), eabf8755. https://doi.org/10.1126/sciadv.abf8755

Yamazaki, K., Aoki, S., Shimada, K., Kobayashi, T., & Kitade, Y. (2020). Structure of the Subpolar Gyre in the Australian-Antarctic Basin Derived From Argo Floats. *Journal of Geophysical Research: Oceans*, *125*(8). https://doi.org/10.1029/2019JC015406

Young-Hyang Park, & Gamberoni, L. (1995). Large-scale circulation and its variability in the south Indian Ocean from TOPEX/POSEIDON altimetry. *Journal of Geophysical Research*, *100*(C12), 24911. https://doi.org/10.1029/95jc01962

Figures and Tables

Figure 1. Circulation and topography in the East Antarctic margin. The 3,000 m isobath is highlighted in white. Polar Front (PF; green), Northern/southern branches of Southern ACC Front (SACCF-N/S; yellow/magenta), and subpolar gyres (blue) are derived from dynamic ocean topography (Section 3.1), and Southern Boundary (SB; red) and Antarctic Slope Front (ASF; cyan) are reproduced from temperature field of a climatological dataset by Shimada et al. (2017). The SACCF-S corresponds to the southernmost eastward jet of ACC (~4,000 m isobath), whereas the SB is located along the center of subpolar recirculating gyres (4,000–3,000 m) about zero lines of zonal velocity.

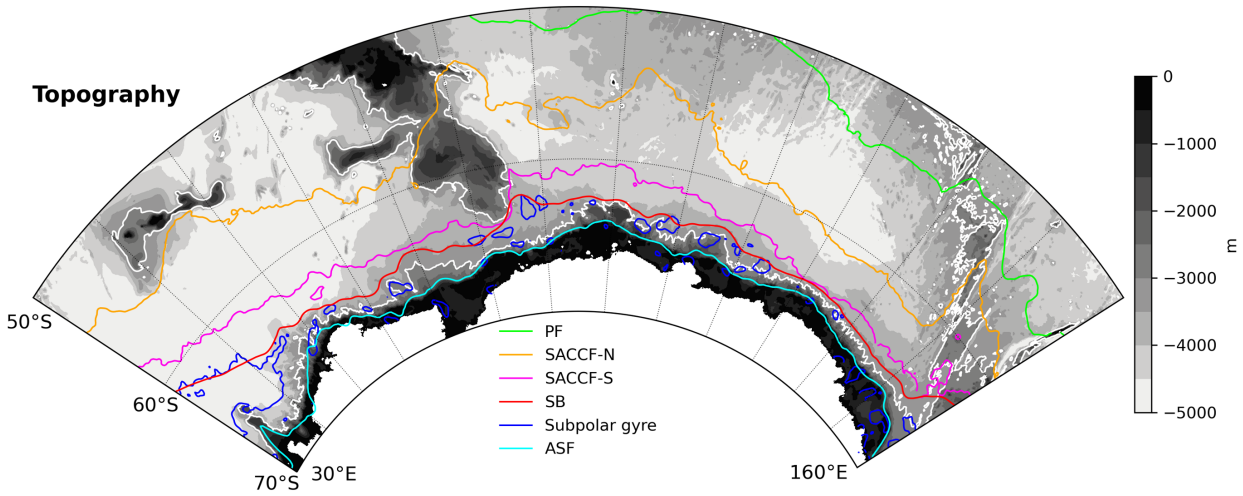

Figure 2. Altimetric flow speed. The upper panel is the mean velocity by surface geostrophy, and the lower panel is the eddy velocity as root-mean-squared speed. Frontal positions are drawn as in Fig. 1.

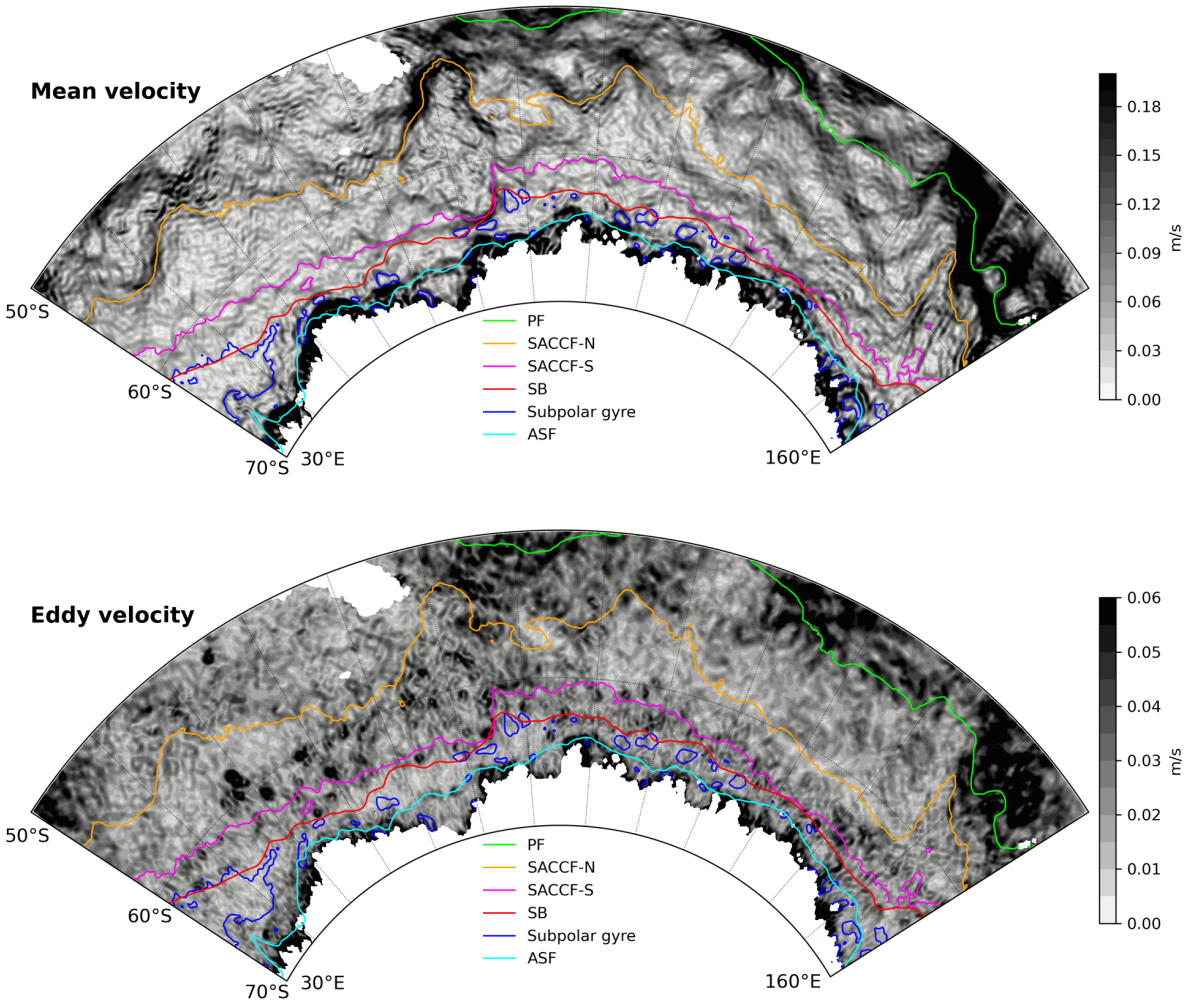

Figure 3. Distribution of hydrographic data and isopycnal watermass properties of ASW and CDW. Data density per 75 km data radius (top), Conservative Temperature (middle), and isopycnal pressure (bottom) are presented for ASW (left) and CDW (right). Areas with less than 10 data points within the 75 km radius are masked in gray. White contours in middle/bottom panels denote isopycnal spiciness/thickness (by 0.05 kg m^{-3}/100 m intervals), respectively, and thick white contour is –0.15 kg m^{-3}/300 m for each panel. SB (red) and isobaths with 1,000 m intervals (black) are also shown.

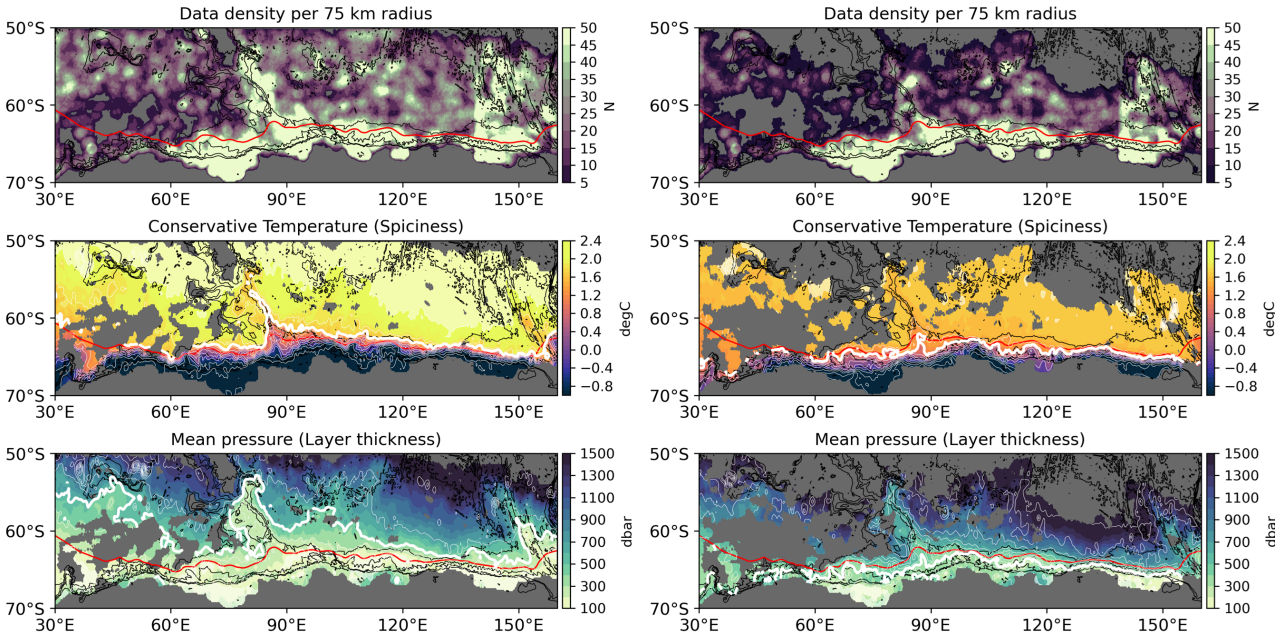

Figure 4. Histogram of mixing efficiency (or correlation coefficient between meridional velocity and temperature) from the cross-slope mooring section in 113°E. "Down-gradient" denotes the correlation by southward velocity, and "up-gradient" means the correlation by northward velocity. Since the downgradient velocity must direct southward (shoreward), "up-gradient" possibly reflects transient events irrelevant to the climatological eddy condition. Hence, in addition to the whole mean (black line) and the previous estimate (dashed line; 0.16), the mean value only for the "down-gradient" is also presented (gray line).

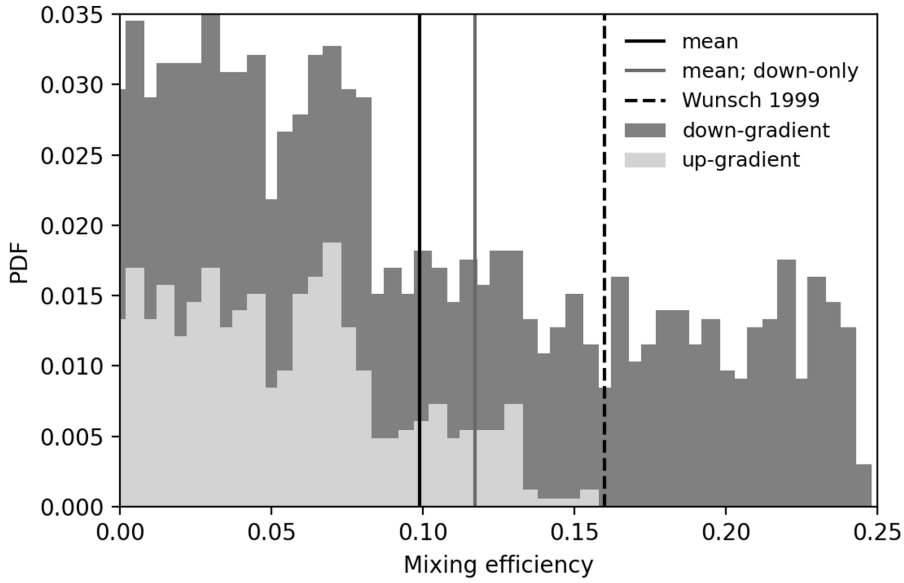

Figure 5. Mixing length calculation using isopycnal spiciness. Spiciness variability (top), normed spiciness gradient (middle), and mixing length (bottom) are presented for ASW (left) and CDW (right). White contours in top/middle panels denote isopycnal spiciness as of Fig. 3.

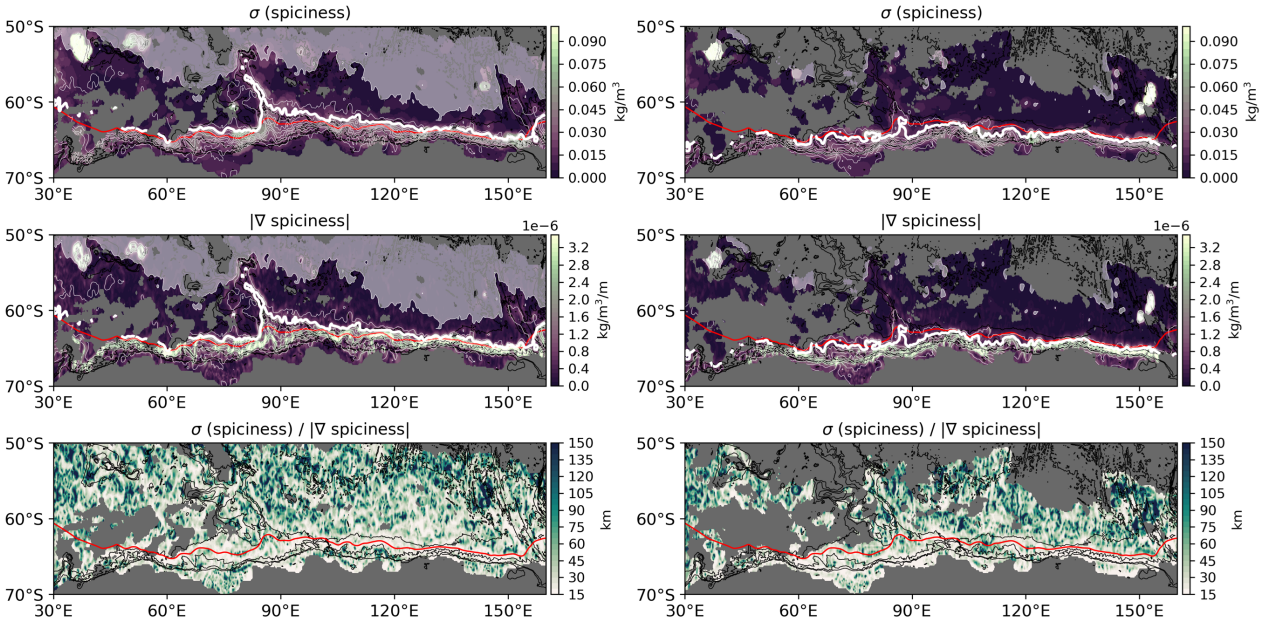

Figure 6. Mixing length calculation using isopycnal thickness. Thickness vari-

ability (top), normed thickness gradient (middle), and mixing length (bottom) are presented for ASW (left) and CDW (right). White contours in top/middle panels denote isopycnal thickness as of Fig. 3.

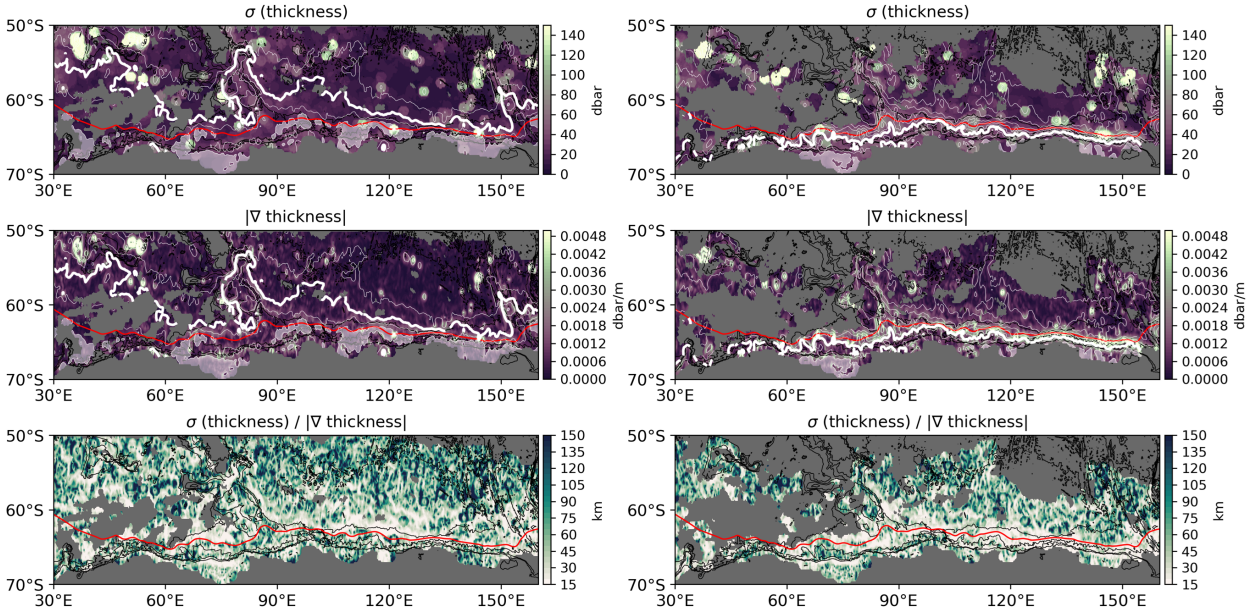

Figure 7. Mixing length dependency on mean flow. Upper and lower panels are based on spiciness and thickness, and left/right panels are for ASW/CDW, respectively. The results are separately shown for the three frontal zones: Subpolar (south of SACCF-S), Southern (from SACCF-S to SACCF-N), and Antarctic (from SACCF-N to PF) Zones. Standard errors due to the spatial variation are shaded.

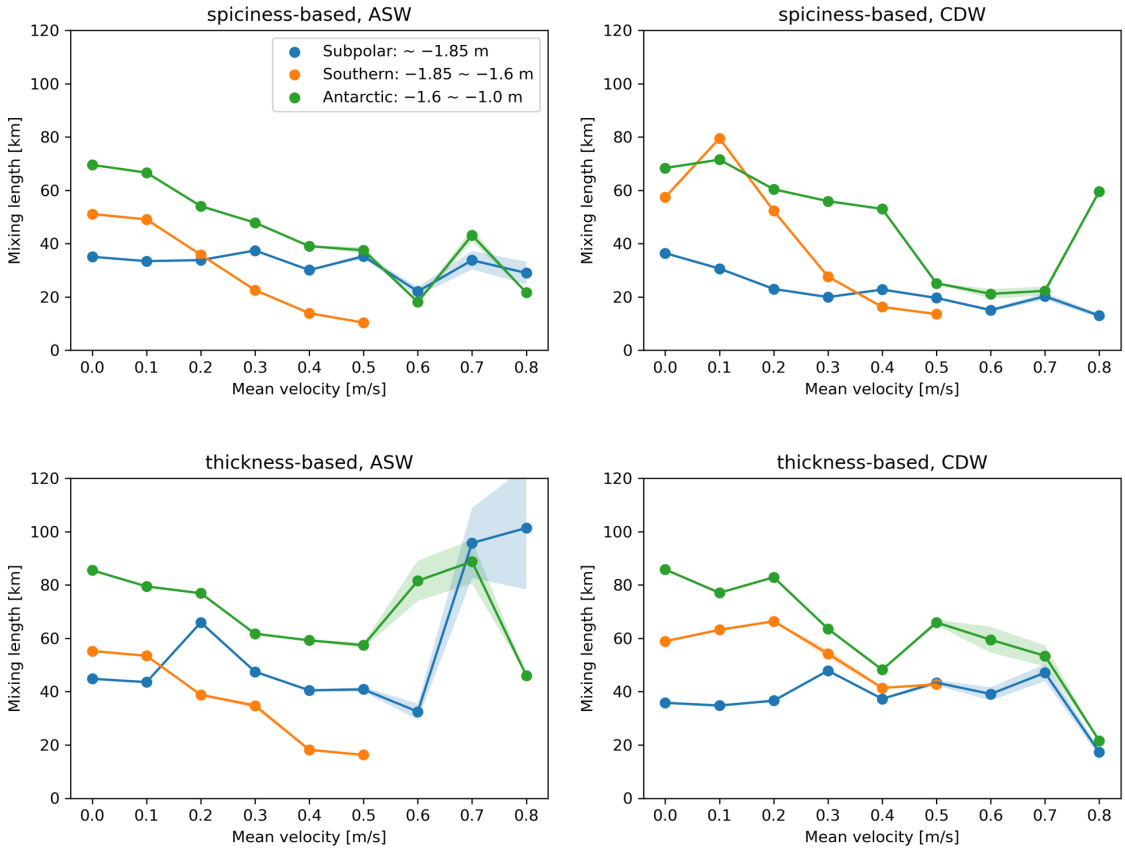

Figure 8. Two-dimensional histogram of mixing length coordinated by tracer variability (horizontal) and inversed tracer gradient (vertical), indicating relative dependency of mixing length on the two variables. Rows correspond to the methods (spiciness and thickness) and layers (ASW and CDW), whereas columns correspond to the three frontal zones. Color shade is normalized to unity, and yellower indicates a larger data population. The axes are also normalized to illustrate their functional dependency. White cross denotes the averaged value of tracer variability and inversed tracer gradient, and white contours are the mixing length of 20 and 100 km. The diagonal dotted line indicates where controls by the two variables become comparable.

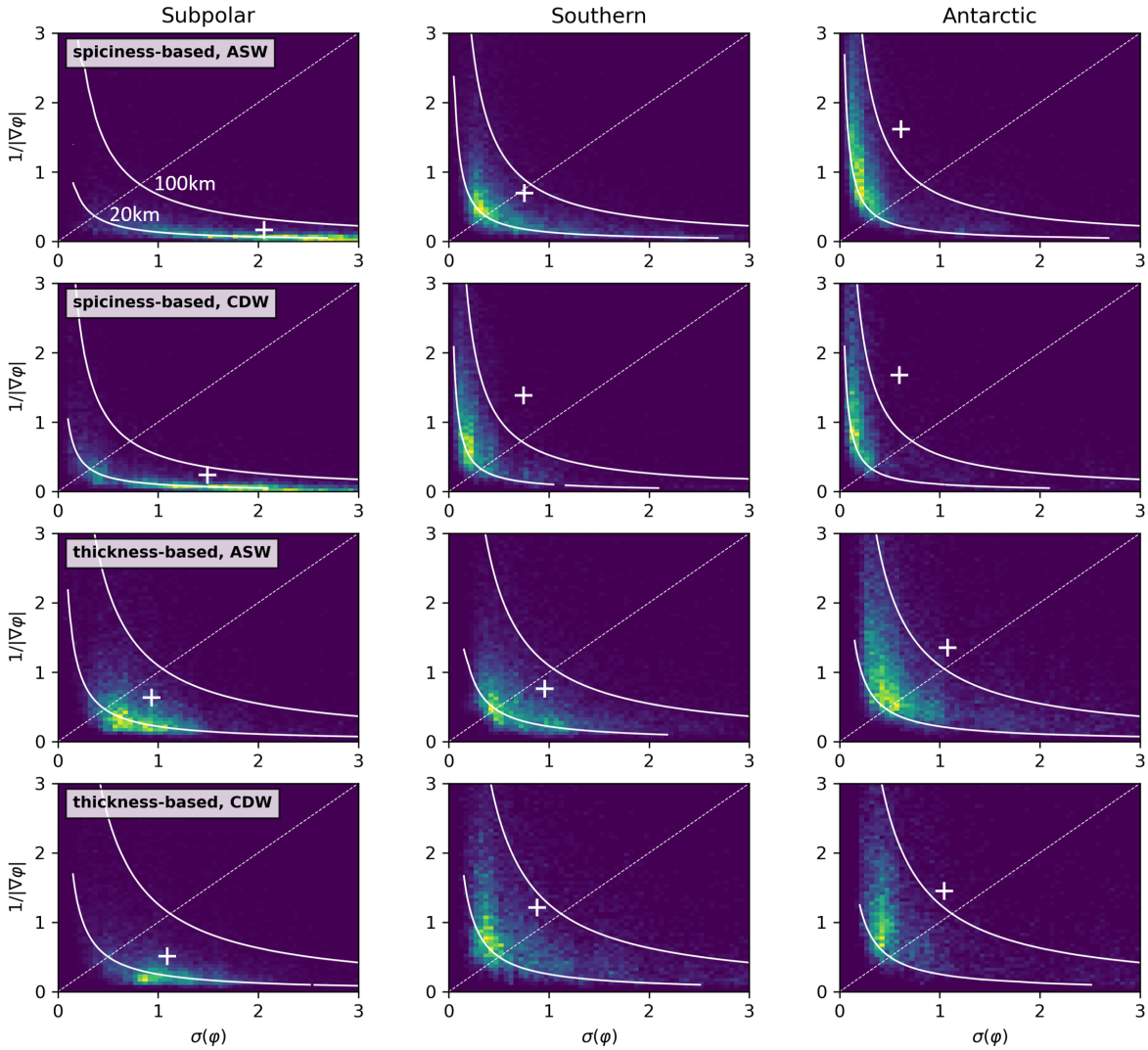

Figure 9. Spatial distribution of isopycnal diffusivity for CDW. Upper and lower panels are based on spiciness and thickness, respectively. In addition to SB (red) and isobaths, dynamic topography is overlaid by 2 cm intervals (white contours). Characteristic contours of dynamic topography are highlighted in blue (thick: subpolar gyre as –1.97 m, thin: SACCF-S as –1.85 m).

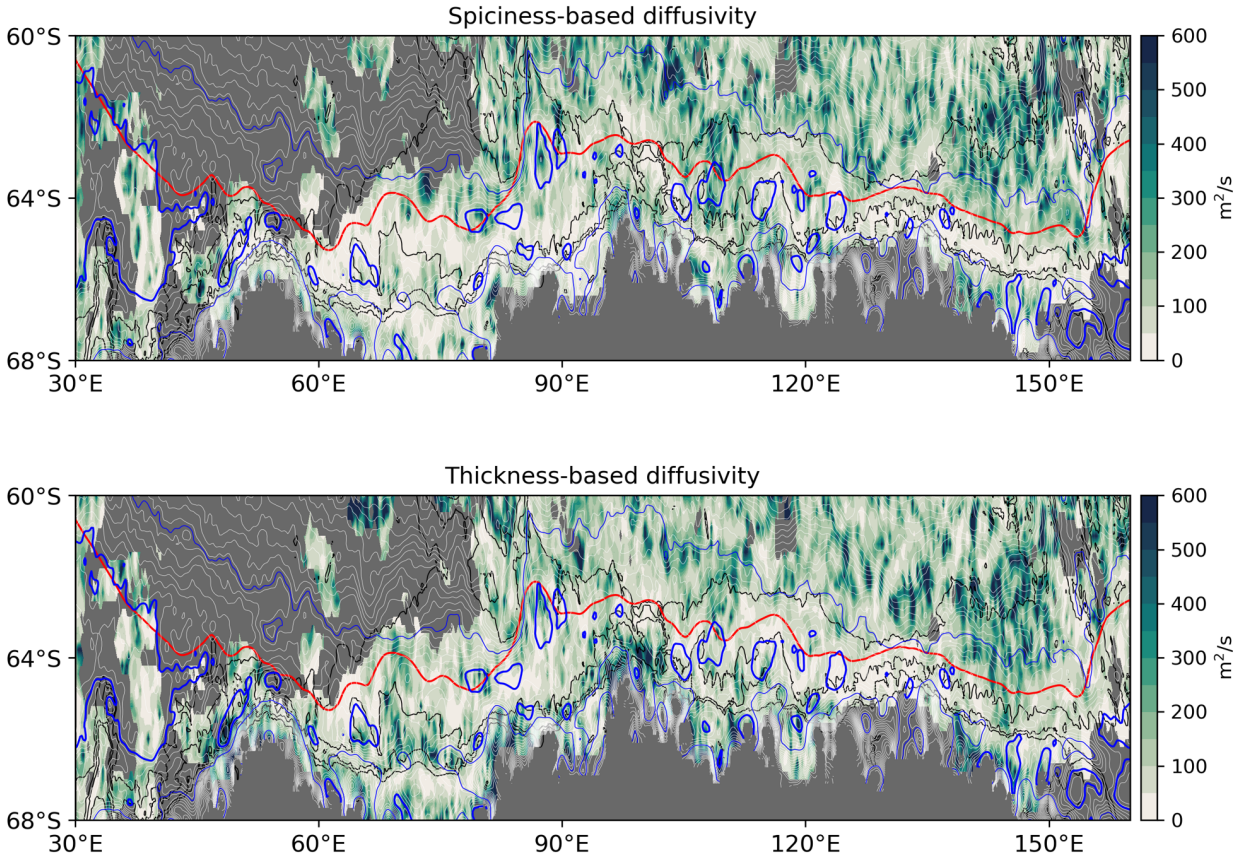

Figure 10. Eddy diffusion and CDW intrusion. Top: same as the lower panel of Fig. 9 (thickness-based diffusivity for CDW), magnified for three continental margins (Prydz Bay, Princess Elizabeth Trough, and off Wilkes Land). Middle: isopycnal CDW temperature (same as Fig. 3, right-middle panel). Vectors annotate where the CDW intrusion well corresponds to the large isopycnal diffusivity. Bottom: schematic of relationship between the eddy flux and CDW intrusion. Continental slope topography controls the barotropic PV field and thus the horizontal structure of subpolar recirculating gyre and intrusion sites.

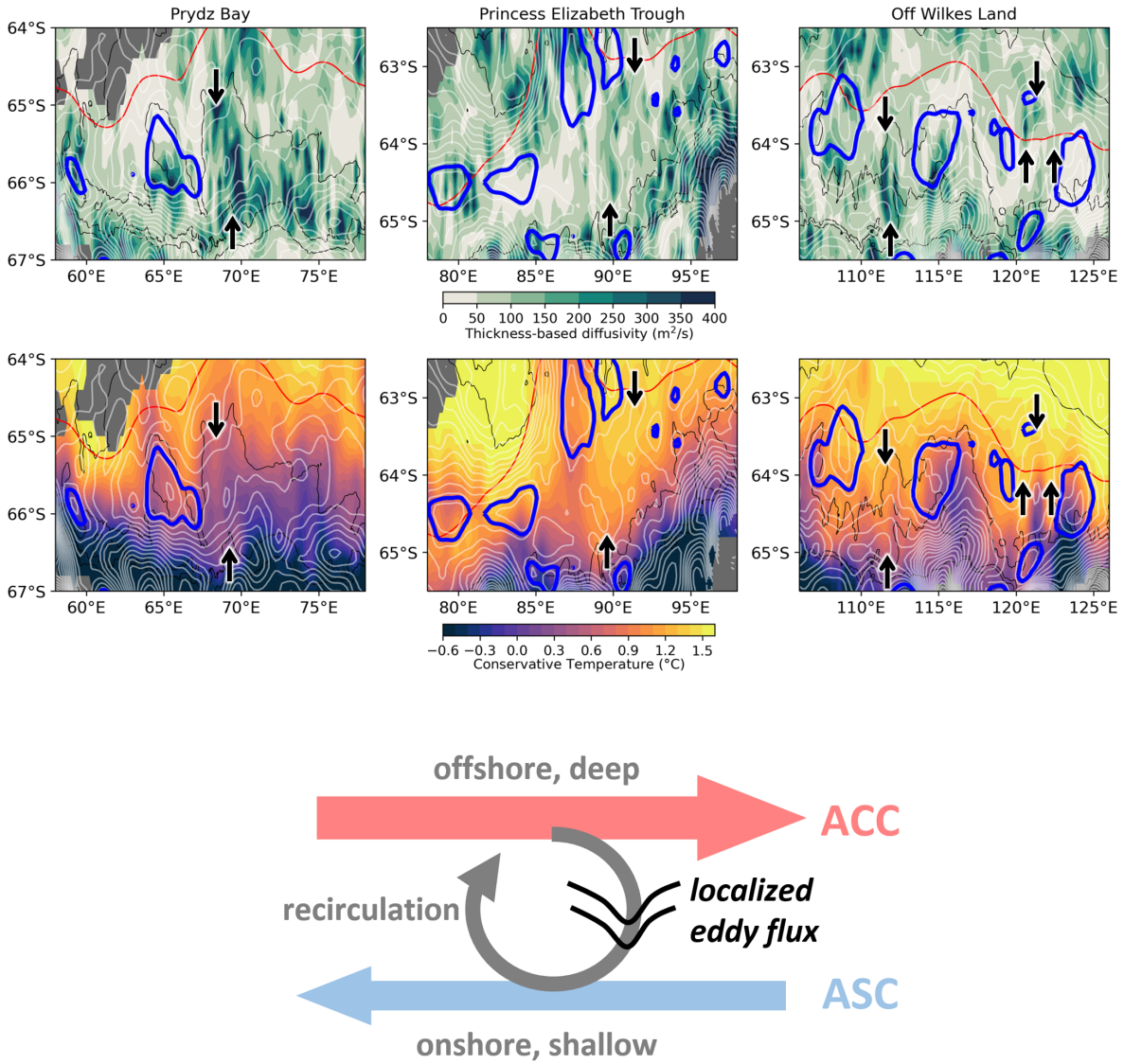

Figure 11. Histogram of isopycnal diffusivity on phase diagram coordinated with eddy velocity (horizontal) and mixing length (vertical), analogously to Fig. 8. White contours denote 100 and 500 m^2 s^{-1}.

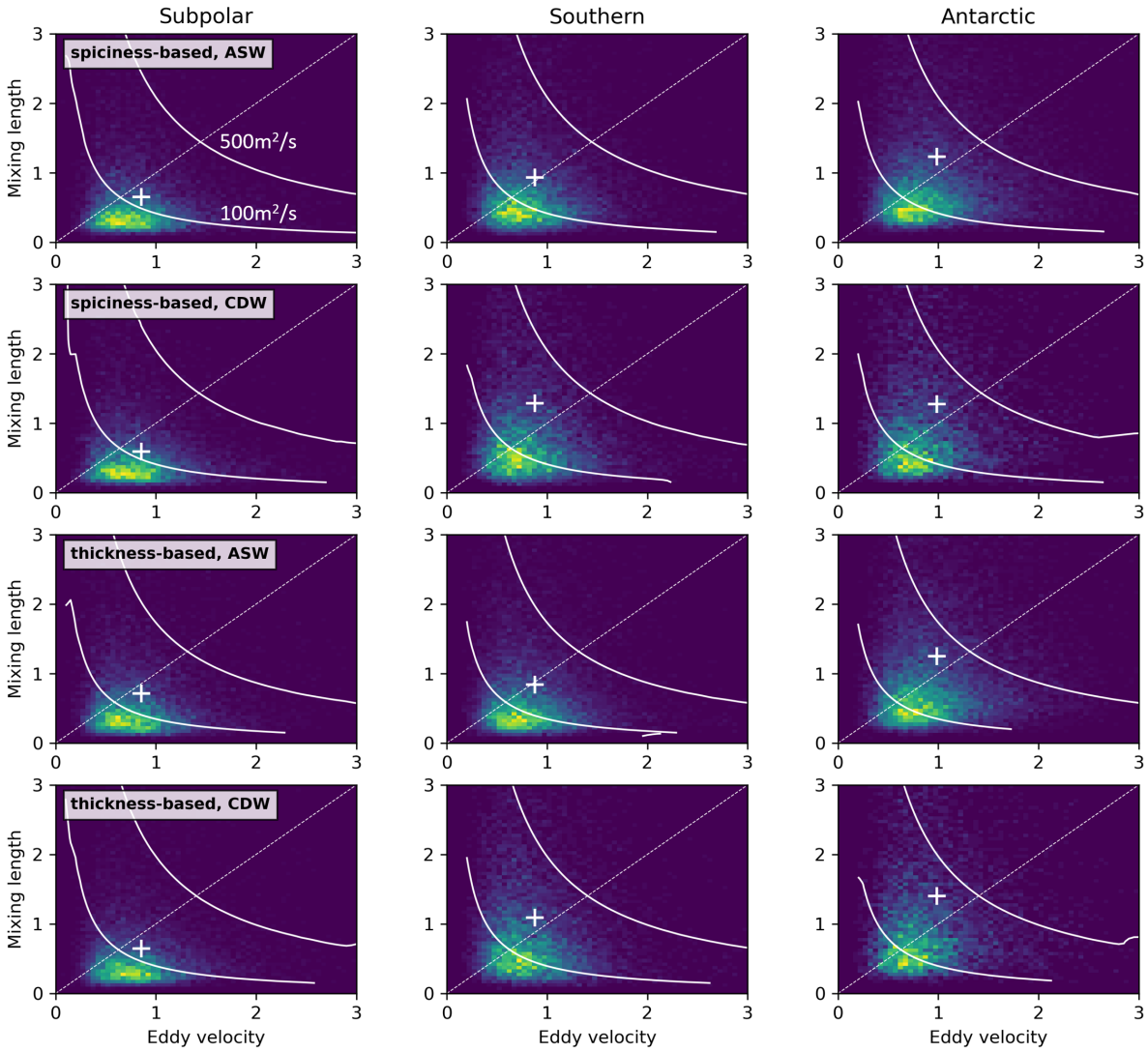

Figure 12. Tracer gradient control of CDW diffusion. Isopycnal diffusivity (top), mixing length (middle), and topographic gradient (bottom) over the 1000–3000 m isobath are regressed onto the inversed tracer gradient as spiciness (left) and thickness (right). Scatters correspond to each grid point, colored by mean flow speed. Horizontal and vertical axes are normalized by the averages.

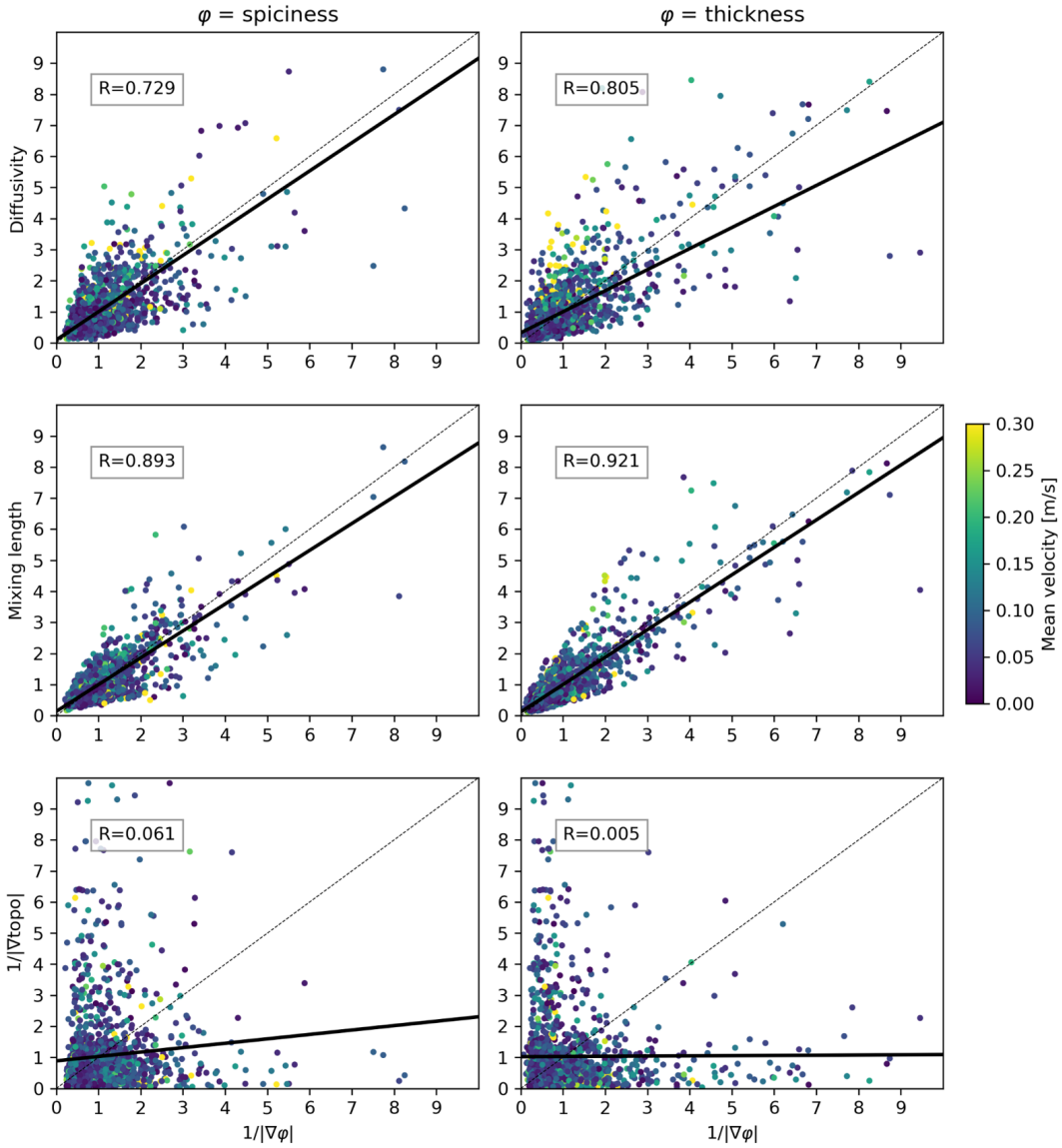

Figure 13. Spatial distribution of Eddy CDW fluxes. The top, middle, and bottom panels are transport vector (with its magnitude), zonal transport, and meridional transport. SB, isobaths, and dynamic topography are denoted as in Fig. 9. For illustrative purposes, colormap for the meridional transport is flipped.

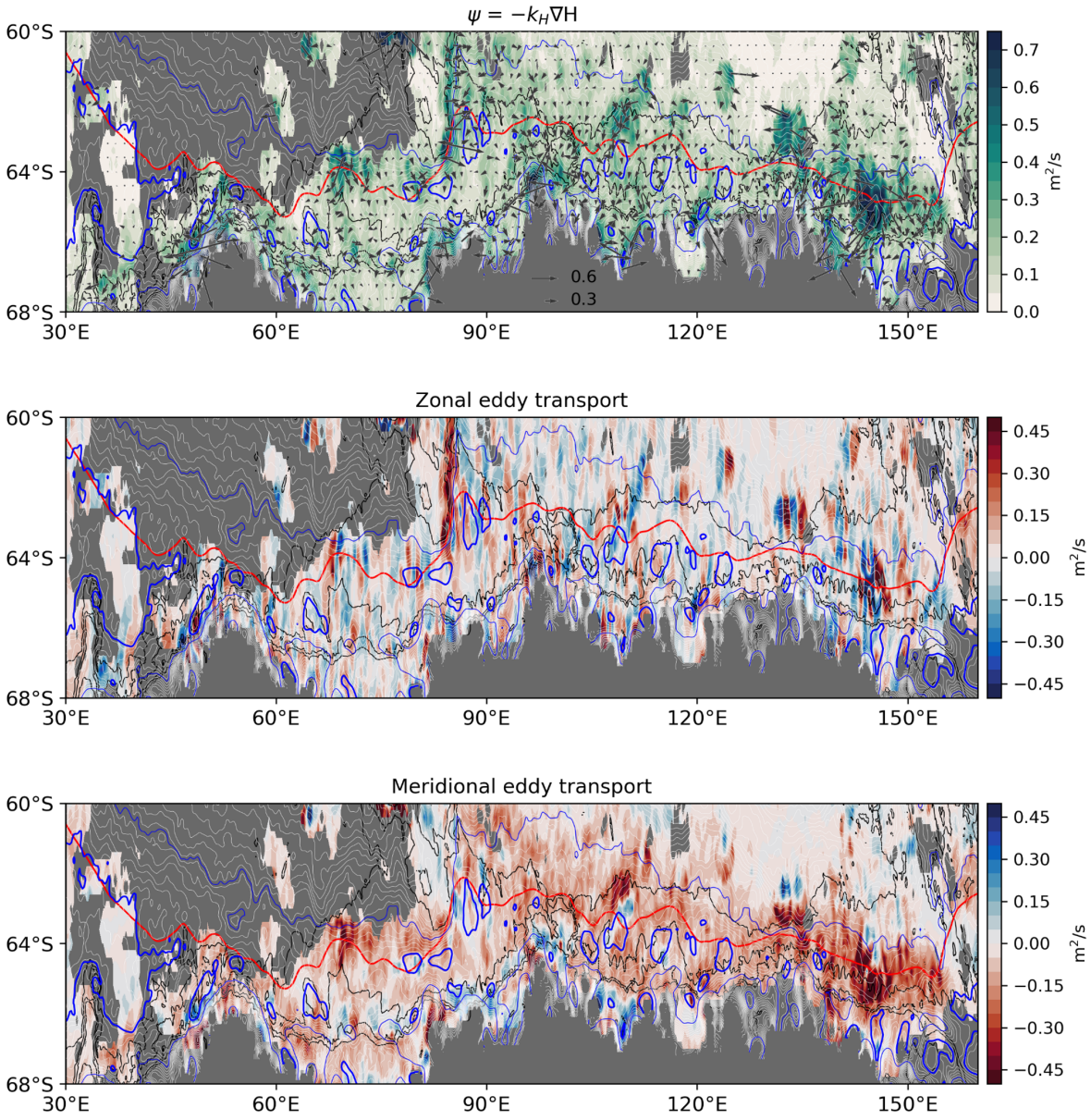

Figure 14. Cross-slope volume/heat transport. Meridional eddy transports for ASW and CDW (averaged within 1° bin in longitude over the continental slope; 1,000–3,000 m isobaths) are zonally integrated. Standard errors due to the cross-slope variation are shown by shade. Volume transport can precisely be translated to heat flux using the mean temperature of CDW and ASW as indicated by ticks to the left. The 90°E meridian for CDW corresponds to

the interbasin boundary between eastern/western Indian sectors, while 130°E is transitional longitude for the ASW transport direction.

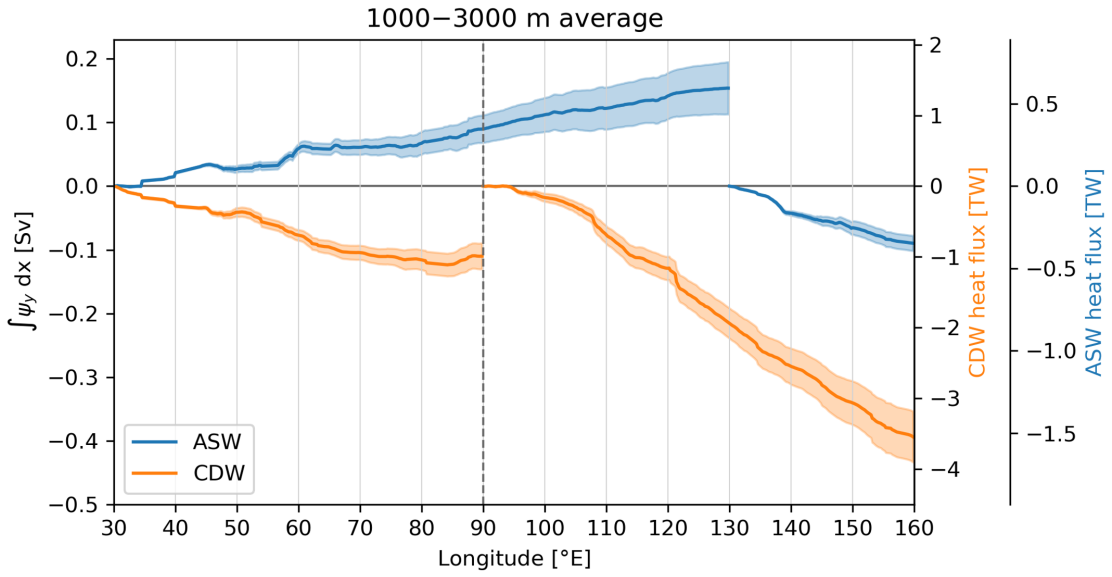

Figure 15. Diapycnal fluxes across CDW. Divergence of isopycnal eddy flux (top) is decomposed into thickness squeezing term (middle) and symmetric diffusion term (bottom). Based on the kinematic analysis, the situation may be summarized as in the right panel, where the isopycnal thickness field primarily controls the isopycnal and diapycnal fluxes.

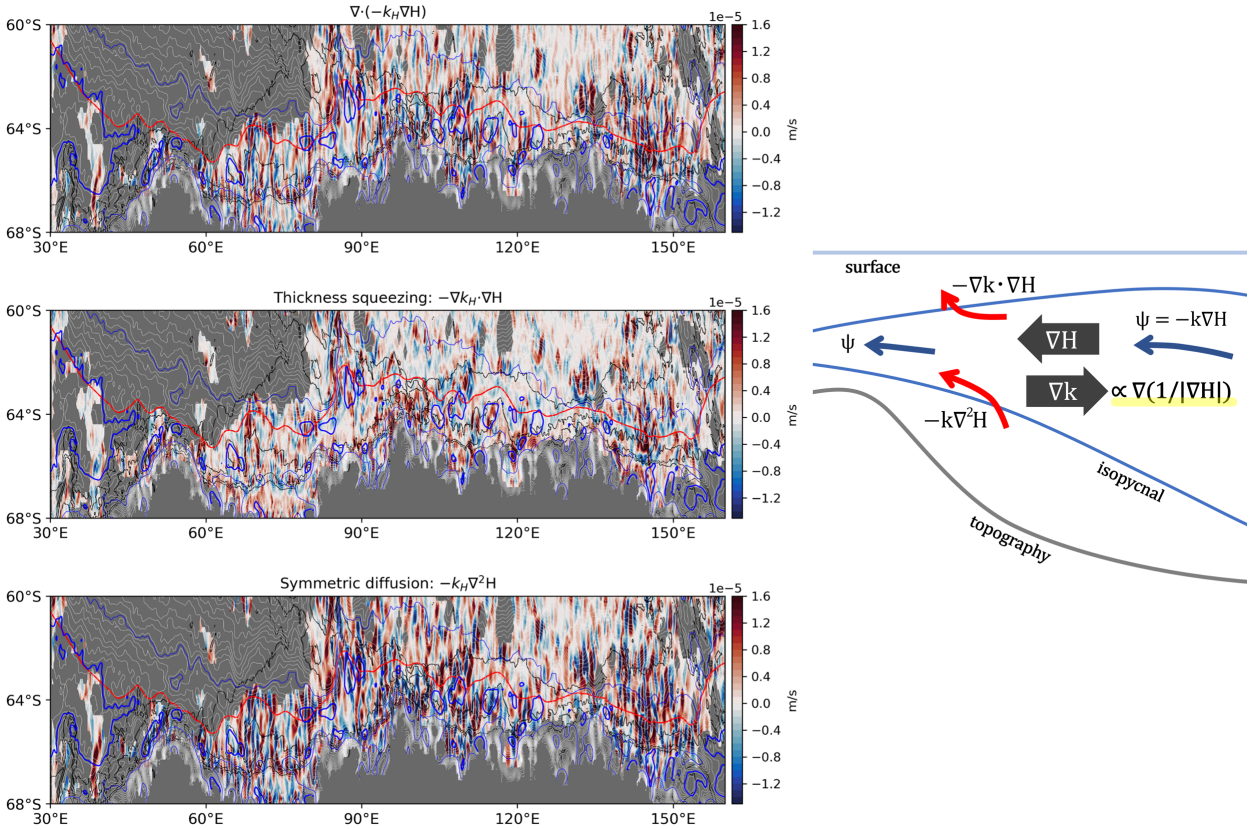

Figure 16. Diffusive CDW flux and isopycnal thickness. Enhanced eddy diffusivity and CDW intrusion are likely associated with small thickness gradient (right), whereas large thickness gradient is associated with suppressed diffusion and strong ASC, hence unintrusive (left).

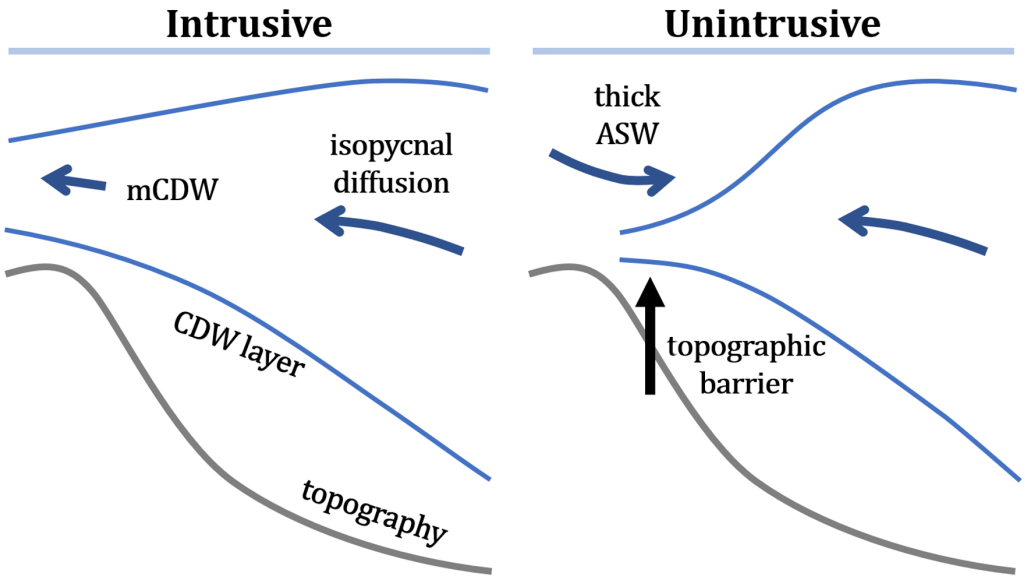
Intrusive
Unintrusive
mCDW
isopycnal
diffusion
CDW layer
topography
thick
ASW
topographic
barrier